Volume 25
DOE/DP40200-19

LLE Review

Quarterly Report

October–December 1985

Laboratory for Laser Energetics
College of Engineering and Applied Science
University of Rochester
250 East River Road
Rochester, New York 14623-1299

Volume 25
DOE/DP40200-19

LLE Review

Quarterly Report

Editor: A. Schmid
(716) 275-3541

October–December 1985

Laboratory for Laser Energetics
College of Engineering and Applied Science
University of Rochester
250 East River Road
Rochester, New York 14623-1299

IN BRIEF

This volume of the LLE Review comprises reports on the performance of the active-mirror-boosted glass development laser (GDL) single-beam system; the implementation of multichannel, soft x-ray diagnostic instrumentation; computer simulation of recent OMEGA laser implosion experiments; materials and ultrafast technology developments in the LLE advanced technology program; and the National Laser Users Facility activities for October–December 1985.

The following are some highlights of the work described in this issue:

- The active-mirror booster stage on GDL brings single-beam, 1054-nm output energy near the kilojoule level for 1-ns pulses.
- Measurements of soft x-ray emission from 100 to 200 eV are now possible with the help of a four-channel, GHz-bandwidth diode spectrometer, which is fully integrated into a digital data acquisition system.
- Comparison of experimental data and predictions of one-dimensional numerical simulations of OMEGA implosion experiments reveal discrepancies that can be resolved by two-dimensional calculations. The consequences of irradiation nonuniformities are well accounted for and required improvements for future experiments are identified.
- The technique of pulse chirping allows simple temporal stretching and recompression operations to be carried out on picosecond

pulses, to amplify such pulses in compact systems and avoid the dangers of optical nonlinearities due to high peak powers.

- High-average-power glass lasers require glasses with improved thermal-shock resistance. Recent gains in ion-exchange surface treatments of a phosphate-composition glass have led to a fivefold increase in thermal-shock resistance for that glass.

CONTENTS

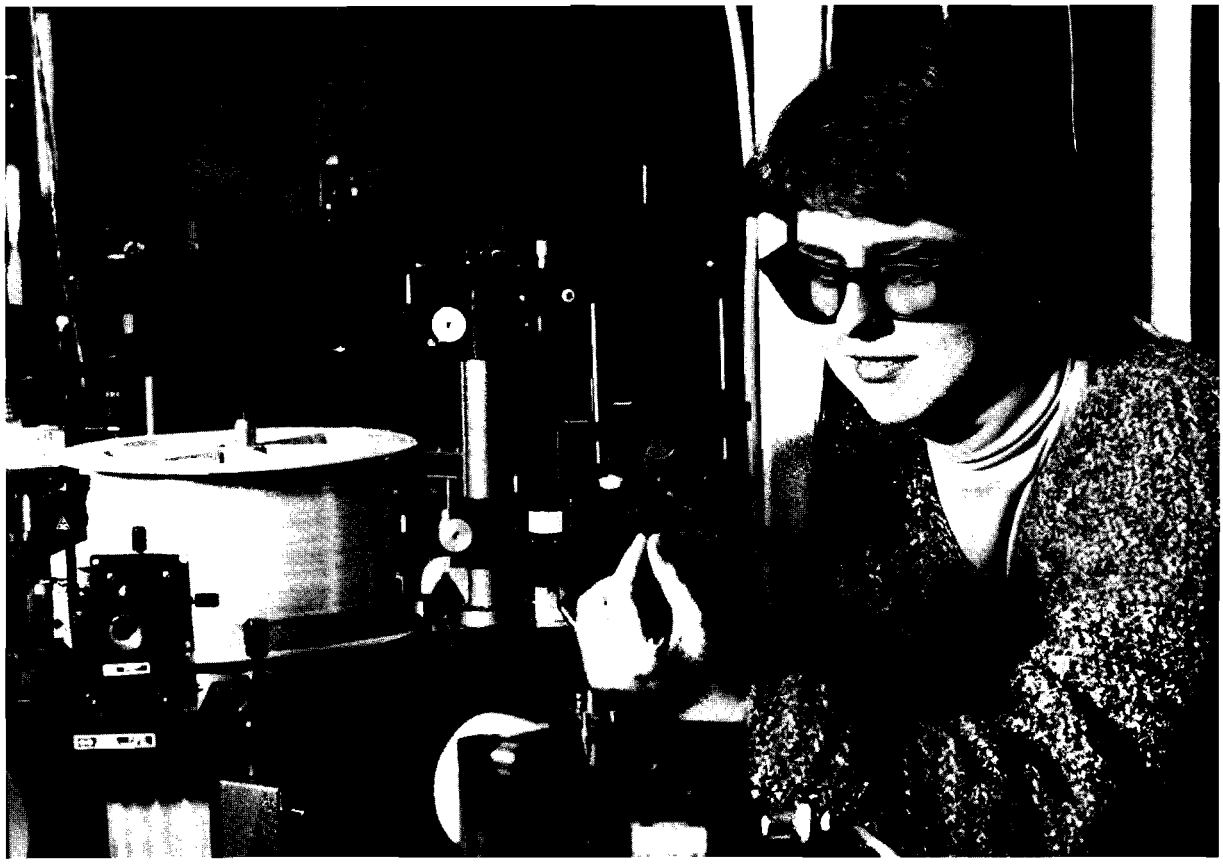

Donna Strickland, a graduate student in optics and a member of the Picosecond Research Group, is shown aligning an optical fiber. The fiber is used to frequency chirp and stretch an optical pulse that can later be amplified and compressed in order to achieve high-peak-power pulses.

Section 1
LASER SYSTEM REPORT

1.A GDL Facility Report

The glass development laser (GDL) system was used for LLE interaction experiments and National Laser Users Facility experiments. The system was also used for beam uniformity studies, the results of which are now being implemented on the 24-beam OMEGA system. In preparation of future experiments, GDL full system output tests at pulse lengths shorter than 1 ns were carried out.

A summary of GDL operations this quarter follows:

System Test Shots		89
Target Shots		49
Pointing, Activation Shots		14
	TOTAL	152

ACKNOWLEDGMENT

This work was supported by the U.S. Department of Energy Office of Inertial Fusion under agreement No. DE-FC08-85DP40200 and by the Laser Fusion Feasibility Project at the Laboratory for Laser Energetics, which has the following sponsors: Empire State Electric Energy Research Corporation, General Electric Company, New York State Energy Research and Development Authority, Ontario Hydro, Southern California Edison Company, and the University of Rochester. Such support does not imply endorsement of the content by any of the above parties.

1.B OMEGA Facility Report

During the first quarter of FY86 a number of improvements and modifications were made to the OMEGA laser system. A comprehensive upgrade of the laser front end took place. An actively mode-locked, Q-switched (AMQ) YLF oscillator, preamplifier, and a reconfigured predriver line were installed. Other activities included a cw system alignment, characterization of a new zoom in-air spatial filter, implementation of liquid-crystal-based polarization devices, and frequency-conversion crystal tuning.

Preparations making GDL a 25th beam of OMEGA for x-ray backlighting purposes are nearing completion. Optical as well as software integration of the two facilities will be completed by the beginning of the second quarter; the first, full-power shots of the GDL beam into the OMEGA target chamber are scheduled to begin in January 1986.

After completion of the system upgrade, OMEGA was used for two experimental programs. The first program, comprising beam uniformity studies, established a data base for beam intensity and phase profiles on selected beam lines. The second, a National Laser Users Facility program and a cooperative project with the Naval Research Laboratory, involved target experiments aimed at vacuum ultraviolet spectroscopy of selected elements.

A summary of OMEGA operations during this quarter follows:

Driver Test and Activation Shots		272
Beamline Test Shots		101
Target Shots		57
	TOTAL	430

ACKNOWLEDGMENT

This work was supported by the U.S. Department of Energy Office of Inertial Fusion under agreement No. DE-FC08-85DP40200 and by the Laser Fusion Feasibility Project at the Laboratory for Laser Energetics, which has the following sponsors: Empire State Electric Energy Research Corporation, General Electric Company, New York State Energy Research and Development Authority, Ontario Hydro, Southern California Edison Company, and the University of Rochester. Such support does not imply endorsement of the content by any of the above parties.

1.C A Kilojoule-Scale Active Mirror System

One year ago LLE revived its interest in the large-aperture, active mirror laser amplifier as a booster for high-power neodymium laser systems. Progress in hardware development involving new mounting and sealing designs had resulted in the successful upgrade of GDL with four 21-cm, clear-aperture, active mirror amplifiers.[1] Lacking the proper front surface coatings on all four mirrors, multiple Fresnel-reflection losses limited the peak energy to just above 300 J at 1-ns pulse width for the single-pass case and precluded effective double-

pass operation of the active mirrors. Furthermore, focusability suffered from the cumulative wave-front distortion caused by each of the mirrors.

Recent progress in fabrication and coating technologies and various assembly and testing techniques has resulted in the successful upgrade of GDL with four fully coated and distortion-free active mirror amplifiers. Interferometric analysis, applied to every stage of fabrication, coating, assembly, and system operation, was central to locating the sources of distortion and in defining effective solutions. Figure 25.1 shows interferograms that represent the optical quality of an active mirror disc at two different steps of the procedure. The interference pattern in Fig. 25.1(a) is generated by a Fizeau interferometer where the active mirror forms the end element in the test arm. The straight vertical fringes show that the unmounted active mirror creates less than a sixth of a wavelength (λ/6) wave-front distortion (λ = 633 nm) in its normal mode of double-pass reflection from its back surface. A Twyman-Green interferogram [Fig. 25.1(b)] of the same disc, following coating, mounting, and sealing, shows a distortion of less than λ/4 (λ = 1064 nm). This measurement is limited by the performance of the interferometer components. Interferometer normalization indeed shows that the distortion is kept below λ/4.

Fig. 25.1
Interferometric testing is an essential part of distortion-free mounting and sealing of the large aperture, active-mirror amplifier disc. The straight, vertical fringes in (a) are generated by a Fizeau interferometer and indicate that the unmounted active mirror creates less than λ/6 wave-front distortion (λ = 633 nm) in its normal mode of double pass reflection from the back surface. A Twyman-Green interferogram of the same disc (b), when coated, mounted, and sealed, shows an accuracy-limited distortion measurement of less than λ/4 (λ = 1064 nm).

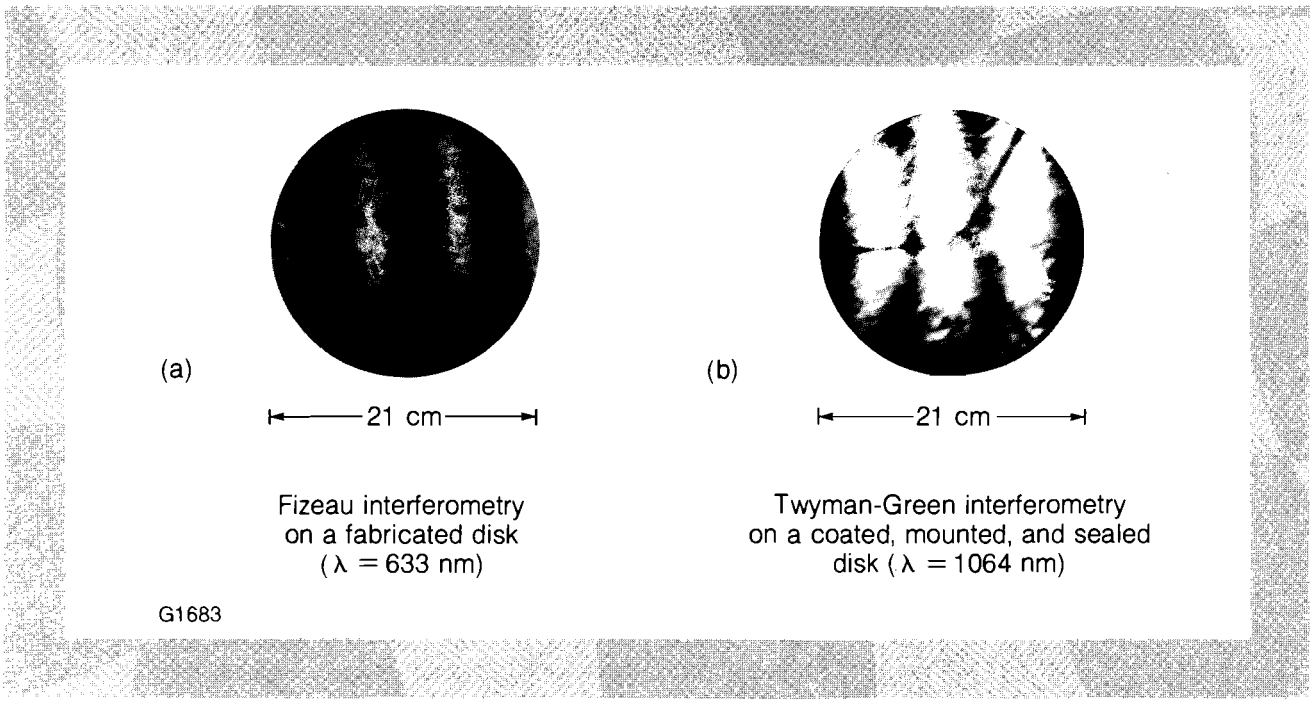

During this GDL upgrade, three of the four active mirrors were reworked to remove old coatings and to repolish surfaces found inadequate because of excessive scratches and digs. Subsequently, each laser disc was coated with an in-house-developed, recently improved front-face dual-purpose coating. This coating simultaneously acts as an antireflection coating at 1054 nm for the front surface, and as a high reflector for the major neodymium pumpbands (Fig. 25.2). This method of returning pump light back into the amplifier increases

the stored energy of a 25×3-cm, LHG-8 active mirror by more than 10%. Coatings of such complex design usually exhibit low damage threshold even at longer wavelengths (1054 nm). Recent tests demonstrate, however, that improved coatings repeatedly withstand irradiance levels higher than 5 GW/cm^2.

This observation supports the belief that removal of subspecification scratches and digs by fine polishing has increased coating adhesion and strength over the entire disk surface.

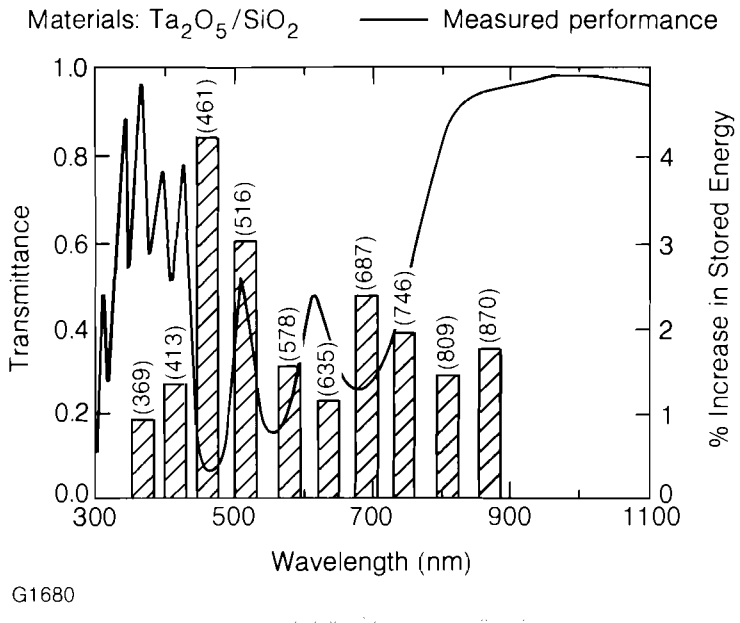

Fig. 25.2
Each active mirror amplifier is equipped with an improved front-surface coating designed to maximize the transmission of the 1053-nm laser beam at the front surface, while simultaneously reflecting the major neodymium pumpbands back into the amplifier. This in-house coating is capable of increasing the stored energy of a 25×3-cm, LHG-8 active mirror by more than 10%.

In an effort to achieve unprecedented high powers in GDL without the risk of damaging optical components, a dedicated effort was made to obtain a uniform-intensity distribution for propagation through the active mirror amplifiers. A thorough investigation of the new oscillator and predriver,[2] as well as of the driver line and remaining rod amplifiers, resulted in smooth spatial intensity profiles, as illustrated by the contour plots of Figs. 25.3 and 25.4. A smooth, Gaussian spatial profile with a slight, 45° orientation characterizes the new predriver in GDL (Fig. 25.3). After several rod amplification stages, which amplify the Gaussian-beam wings most prominently by the characteristic edge-gain profile, the energy distribution at the input to the active mirror booster remains smooth, center peaked, and at a slight, 45° orientation [Fig. 25.4(a)].

Accurate alignment techniques implemented throughout the laser chain have resulted in highly uniform active mirror intensity distributions [Fig. 25.4(b)] at very high-peak-power levels. Figure 25.5 shows the 500-ps performance of the single-passed active mirrors in GDL. The experimental results exceeded theoretical predictions by

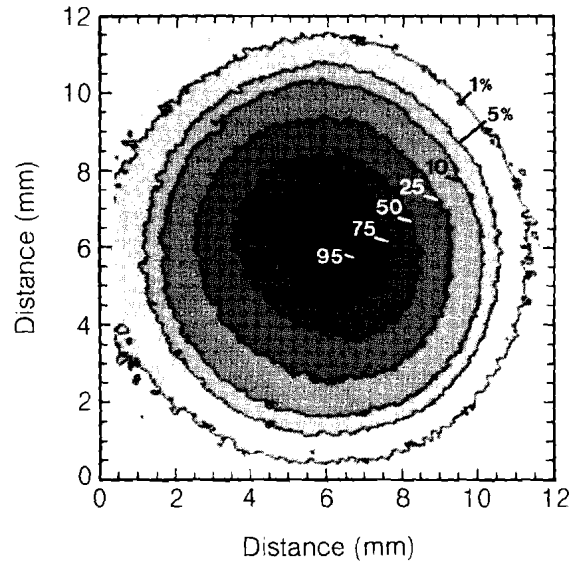

G1681

Fig. 25.3
Uniform spatial intensity distributions are essential for damage-free, high-power scaling of LLE laser systems. A smooth Gaussian spatial profile with a slight, 45° orientation characterizes the new predriver output in GDL.

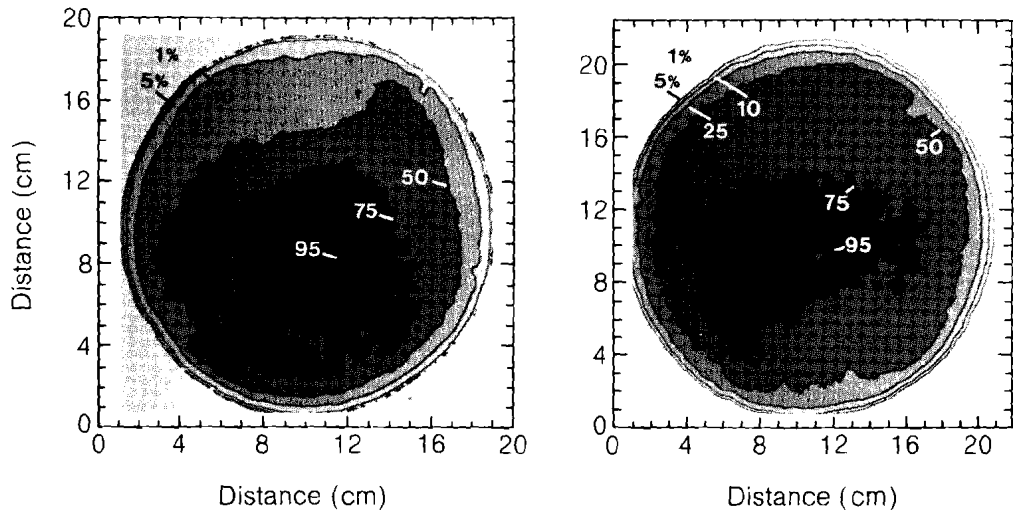

(a) Active Mirror Input Near Field (b) Active Mirror Output Near Field

G1682

Fig. 25.4
After several rod amplification stages, the energy distribution at the input to the active mirror booster remains smooth, center peaked, and at a slight, 45° orientation (a). Accurate alignment techniques used throughout the laser chain result in highly uniform active mirror outputs (b).

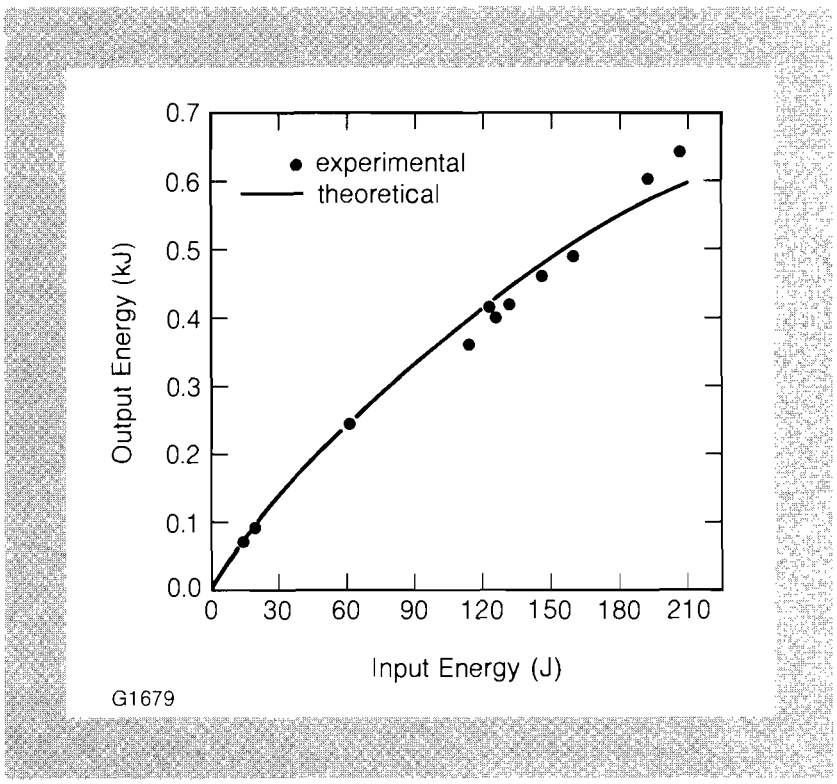

Fig. 25.5
Performance of a four-unit, single-passed active mirror booster to the glass development laser (GDL) at 500 ps. Experimental results exceeded theoretical predictions to produce more than 1 TW of focusable power.

the code *RAINBOW* and yielded more than 1 TW of focusable power. Higher powers can only be obtained in a double-pass configuration, since the system is clearly driver limited at this point.

The active-mirror-boosted GDL facility is currently scheduled for more extensive beam characterization, as it delivers 100-ps pulses for short-pulse frequency tripling in x-ray backlighting experiments and 500-ps to 1-ns pulses for frequency-doubled interaction experiments.

ACKNOWLEDGMENT

This work was supported by the U.S. Department of Energy Office of Inertial Fusion under agreement No. DE-FC08-85DP40200 and by the Laser Fusion Feasibility Project at the Laboratory for Laser Energetics, which has the following sponsors: Empire State Electric Energy Research Corporation, General Electric Company, New York State Energy Research and Development Authority, Ontario Hydro, Southern California Edison Company, and the University of Rochester. Such support does not imply endorsement of the content by any of the above parties.

REFERENCES

1. LLE Review **21**, 3–7 (1984).
2. LLE Review **20**, 143–149 (1984).

Section 2
PROGRESS IN LASER FUSION

2.A Numerical Simulation of Recent, 24-Beam, Blue (351-nm) OMEGA Implosion Experiments

LLE is presently involved in a series of experiments intended to demonstrate the ability of direct-drive laser fusion to ablatively compress microencapsulated deuterium-tritium (DT) fuel to 200 times its liquid density. This campaign has been structured into three parts. The first part was initiated in February 1985 and involved the implosion of glass microballoons filled with various pressures of DT gas. Compression of these initial targets attained maximum fuel densities of 6.0 to 6.5 g/cm^3, or ~30 times liquid DT density (30 XLD) and maximum neutron yields in the range of 1.5 to 2.0 × 10^{11}. The experiments also served to test recently added diagnostics on the OMEGA system which will be necessary to evaluate the final 200-XLD targets. These diagnostics include knock-on fuel ion spectrometry for measuring fuel areal density ($<\rho R>$),[1] radiation chemistry techniques (RAD-CHEM) for measuring shell areal densities ($<\rho\Delta R>$),[2] neutron time-of-flight equipment for determining core temperatures,[3] and Kirkpatrick-Baez (K-B) microscopes, which give spatially resolved x-ray emission information from the imploding shell.[4]

The second phase of the 200-XLD campaign is to begin in January 1986. Because of the unavailability of cryogenic targets, this phase will involve the use of targets similar to those in the first phase, and high-pressure (100- to 150-atm), DT-filled glass microballoons. One-dimensional simulations show that the implosion characteristics (e.g., convergence ratios) of small-diameter, high-pressure targets resemble those of targets using moderately thick layers of cryogenic fuel. As such,

these "surrogate cryogenic" targets will provide preliminary information concerning the implosion of cryogenic targets. Furthermore, because the small diameters of these targets will result in high illumination intensities (i.e., $>2 \times 10^{15}$ W/cm^2), these targets might provide experimental data reflecting the presence of certain plasma physics processes (e.g., $2\omega_p$, self-focusing, etc.) in the underdense corona. Finally, should the fabrication of bare plastic shells containing thick layers of cryogenic DT fuel prove difficult, these high-pressure, glass-shell targets will be frozen and used in the final phase of the 200-XLD campaign.

The third and final stage of the 200-XLD campaign, expected to be initiated in the summer of 1986, involves the use of cryogenic DT fuel overcoated with plastic shells. It is through the compression of these cryogenic targets that the expected goal of fuel densities in excess of 200 XLD is to be achieved.

This article presents comparisons between numerical simulations (both one- and two-dimensional) and recent experimental results obtained from the initial phase of the 200-XLD campaign on the OMEGA system. The numerical simulations were carried out using the one-dimensional hydrodynamics code, *LILAC*,[5] and the two-dimensional hydrodynamics code, *ORCHID*. Both codes, which were developed at the University of Rochester, are based on a one-fluid, two-temperature approximation employing the use of Lagrangian hydrodynamics. The calculations include (1) tabular equation of state (SESAME[6]), (2) flux-limited electron thermal transport,[7] (3) multifrequency-group radiation transport using LTE opacities reduced from the LANL Astrophysical Library,[8] and (4) the use of geometrical optics ray tracing[9] for the deposition of laser energy by inverse bremsstrahlung. Emphasis is placed on comparison between experiment and simulation in neutron yields, fuel and shell areal densities, and x-ray emission images.

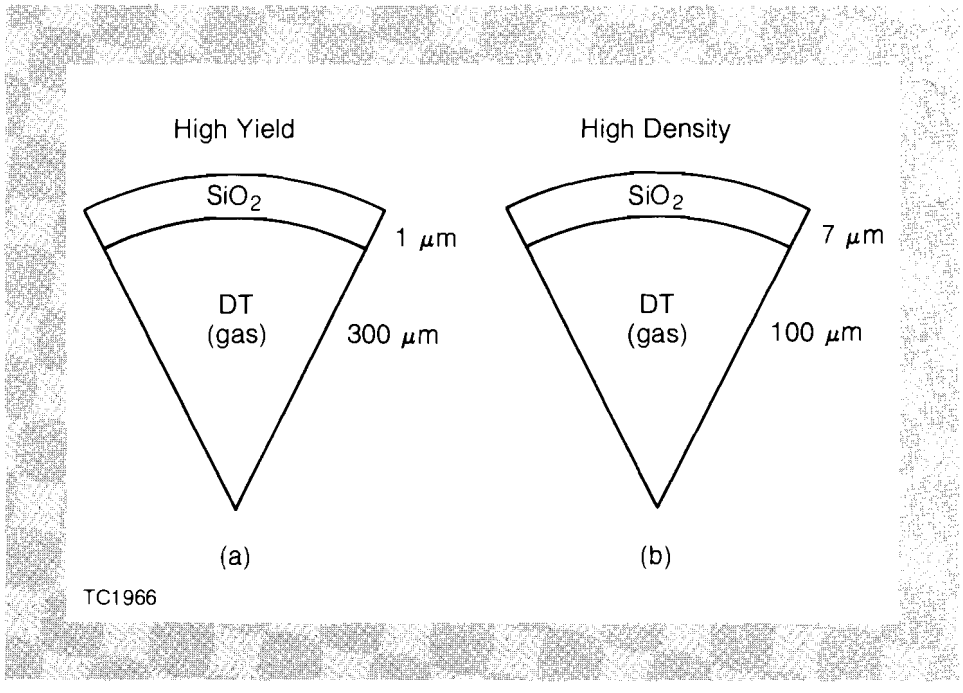

Fig. 25.6
2.0-kJ generic target designs used for attaining (a) high yield and (b) high density. Both designs call for initial fuel pressures of 10 atm.

Target Design Overview

Preliminary scoping studies[10] were performed to identify candidate target designs for use in the initial phase of the 200-XLD campaign. The two basic designs that emerged from this work are shown in Fig. 25.6. The first of these designs [Fig. 25.6(a)] is intended to maximize neutron yield. Optimal performance of such targets requires that the target shell be accelerated to high velocities that will, upon stagnation at the center of the pellet, produce high core temperatures. Therefore, these targets have large initial diameters that maximize the absorbed laser energy and use thin (low-mass) shells to maximize the resulting shell velocity. The simulated behavior is represented in Fig. 25.7.

Viewing the radius versus time (R-T) plot shown in Fig. 25.7(a), it should first be noted that this target is being driven ablatively rather than explosively. In an exploding pusher, the shell blows apart, with roughly half the mass moving out and the other half moving toward the center. In an R-T plot for such an implosion, the half-mass point within the shell (approximately the shell midpoint) would remain relatively motionless until after the imploding part of the shell rebounds. For ablatively driven targets, the driving force is not generated at the shell midpoint but at the ablation surface near the outer edge of the shell. As such, the ablation process "peels away" the outer layers of the shell while accelerating the remaining mass inward. Although most of the shell mass is initially accelerated inward, less than half remains by the time the shell reaches stagnation. Neither the mass of the imploding shell nor the position of the shell midpoint remains constant during the implosion for ablatively driven targets.

One-dimensional simulations show that the glass-fuel interface velocity, illustrated in Fig. 25.7(b), easily exceeds 4×10^7 cm/s, and in some cases approaches 6×10^7 cm/s. These high-velocity shells produce high core temperatures as a result of shock heating and shell stagnation. The simulated neutron energy spectrum is shown in Fig. 25.7(c). Applying the prescription put forth by Brysk,[3] the neutron-averaged ion temperature for this implosion was ~5.0 keV. The neutron spectrum was integrated and gave a neutron yield of $\sim 1.60 \times 10^{12}$ neutrons. Both of these results are consistent with results from the overall simulation. Although such yields are quite encouraging, the corresponding maximum densities are low. The temporal density profile is displayed in Fig. 25.7(d), showing a maximum fuel density of only 0.89 gm/cm^3, corresponding to ~ 4 XLD.

The second type of design [Fig. 25.6(b)] is intended to maximize the compressed fuel density. This type of target requires that increases in the fuel temperature due to nonisentropic processes (e.g., shock preheat) be kept as low as possible, providing a relatively massive inward-moving shell with minimal resistance in compressing the fuel to high densities. These targets require the use of small diameters to limit the distance over which the acceleration can act, and of relatively thick shells to lower implosion velocities. The simulated behavior is shown in Fig. 25.8.

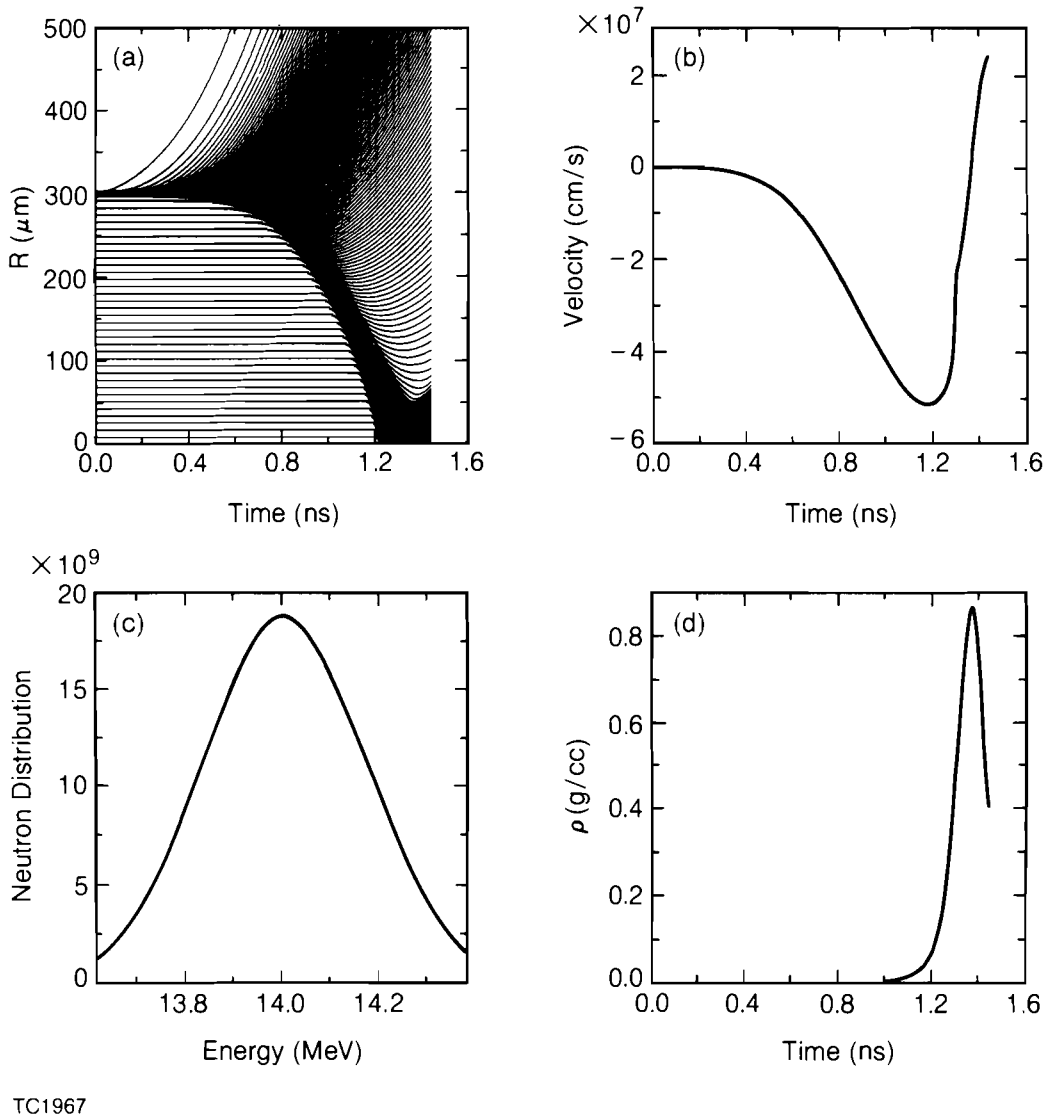

Fig. 25.7
One-dimensional LILAC *simulation of a high-yield target:*
(a) R-T plot,
(b) interface velocity history,
(c) neutron energy spectrum, and
(d) fuel density history.

As before, the R-T plot [Fig. 25.8(a)] shows that this target is being ablatively driven. An additional feature is that a slight shock breaks out of the interior surface of the glass shell because of the lower velocity achieved by these targets. The lower velocities [between 1 and 2 × 10^7 cm/s, shown in Fig. 25.8(b)] produce only modest temperatures (1–2 keV), allowing the incoming shell to compress the fuel on a much lower adiabat to high densities. The analysis of the predicted neutron energy spectrum [Fig. 25.8(c)] illustrates the generation of only modest temperatures. This spectrum shows the neutron-averaged temperature to be ~ 1.6 keV and the neutron yield to be 1.00 × 10^{10}. Because of the low temperatures, the maximum fuel density predicted [Fig. 25.8(d)] is 45 g/cm^3, or 210 XLD.

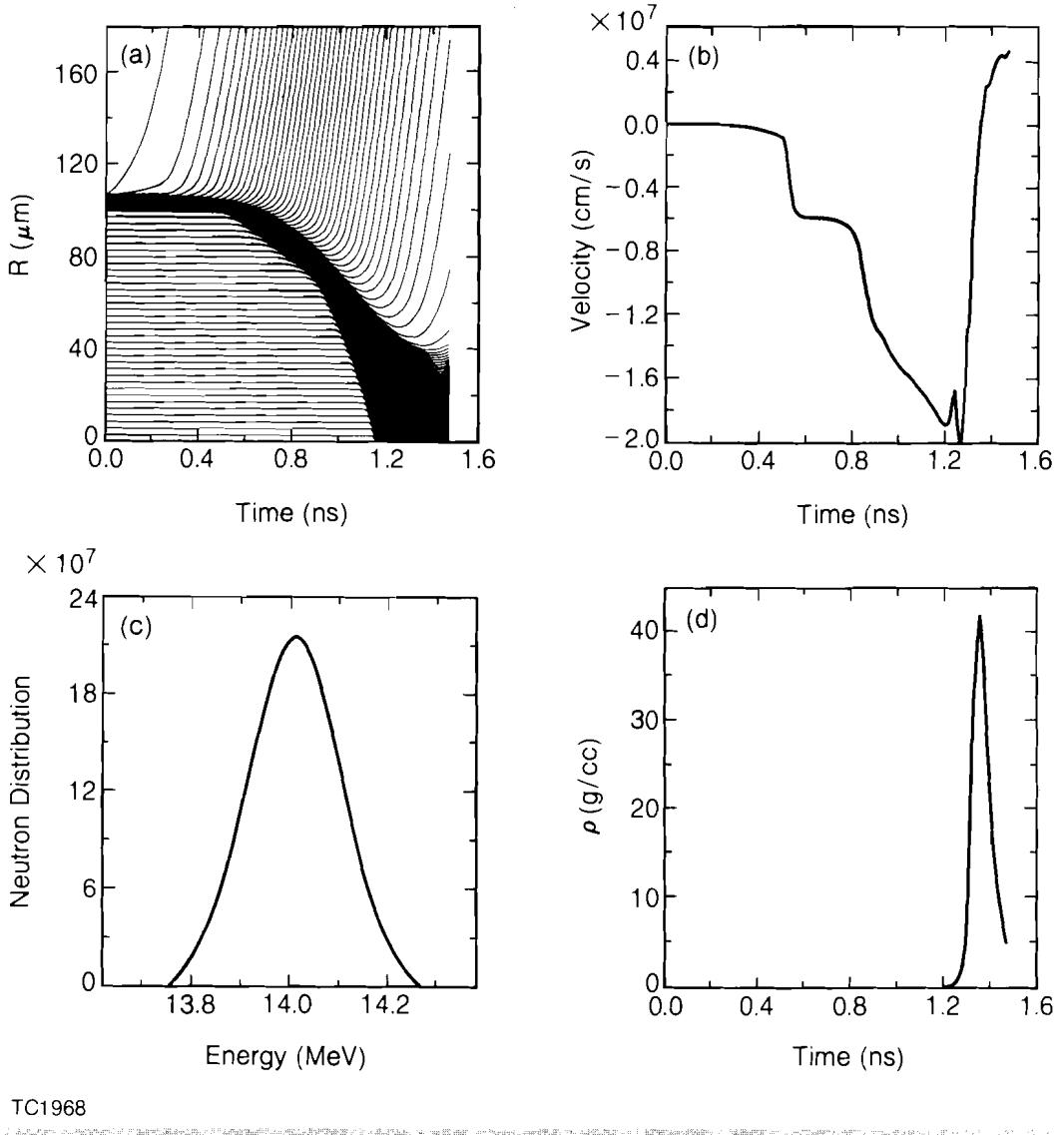

Fig. 25.8
One-dimensional LILAC *simulation of a high-density target:*
(a) R-T plot,
(b) interface velocity history,
(c) neutron energy spectrum, and
(d) fuel density history.

In summary, the targets used for the initial phase of the 200-XLD campaign fell into two categories. The first, high yield, was necessary to provide neutrons for testing new diagnostics to be used in the analysis of the final 200-XLD cryogenic target implosions. The other category, high density, was designed to maximize fuel density and provides an initial setting from which the final goal of 200 XLD can be achieved.

Experimental Comparison

The initial sequence of experimental implosions on the 24-beam, blue (351-nm), 2-kJ OMEGA laser system was completed in June 1985.[11] In conjunction, there was a significant numerical-simulation campaign, in both one and two dimensions, designed to provide additional insight

into the interpretation of the experimental results. Particular interest has been paid to the comparison of overall neutron yields, fuel and shell areal densities, and x-ray microscope film response curves.

The comparison between experimental and predicted neutron yields has traditionally been displayed as a function of the initial glass shell thickness. When applied to the large number of significantly different target designs involving different initial aspect ratios, initial fill pressures, and the occasional use of plastic overcoats, however, this relationship failed to provide any useful insight into this series of implosions. A more meaningful display of the comparison between the experimental and predicted neutron yield was found in terms of the one-dimensional predicted convergence ratio. (Here the convergence ratio is defined as the ratio of the initial fuel radius divided by the fuel radius of the stagnated core.) This relationship was further simplified by normalizing the experimental yields to the corresponding one-dimensional prediction. Results are shown in Fig. 25.9.

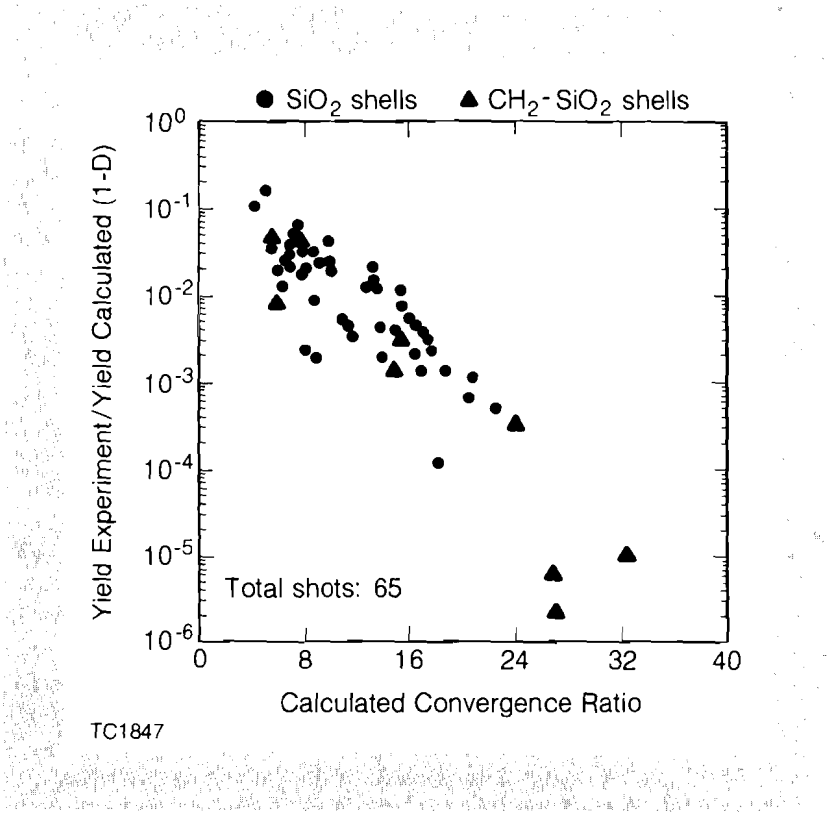

Fig. 25.9
Experimental neutron yields, normalized to the calculated one-dimensional yield, drawn as a function of the calculated convergence ratio.

In Fig. 25.9, the strong dependence of the normalized neutron yield on the predicted convergence ratio is clearly evident. This graph shows that experiments with targets requiring high predicted convergence ratios (i.e., 15–30) performed very poorly in comparison with one-dimensional simulations. The declining agreement with increased predicted convergence ratio suggests the possible presence of implosion nonuniformities. The presence of these nonuniformities would be expected to disrupt the compressed core and prematurely terminate the thermonuclear burn. As a result, the neutron-weighted diagnostics (i.e., knock-on ion spectrometry and RAD-CHEM techniques) would give

physical information that no longer corresponds to the time of peak compression but rather to an earlier time corresponding with the termination of burn. In Fig. 25.10, the measured fuel and shell areal densities are compared with the areal densities at those times in the simulations when the neutron yields equal the total experimental yields. At these points in the implosions, Fig. 25.10(a) shows agreement between the experimental and simulated fuel $<\rho R>$ values over the range of predicted convergence ratios. However, the shell $<\rho R>$ comparison, illustrated in Fig. 25.10(b), shows that the experiments achieve higher values than the simulations as the convergence ratio is increased. The different behavior of the fuel and shell areal-density comparisons can again be explained by the existence of nonuniformities in the target. At this point in the implosion, the fuel $<\rho R>$ is dominated by volume changes in the core due to the imploding shell. Although the shell is deformed, the difference in volumes between the perturbed and unperturbed cases is small and, as such, the experimental and simulated fuel $<\rho R>$ values should be in agreement. The shell $<\rho \Delta R>$ values, however, are very sensitive to distortions in the shell. Because deformations in the shell cause increased compression, the measured shell $<\rho \Delta R>$ values would be higher than those predicted by the simulation. It is important to point out, therefore, that attempts to infer core conditions (e.g., fuel density) from the measured shell areal density can give incorrect results if care is not taken to analyze the entire implosion.

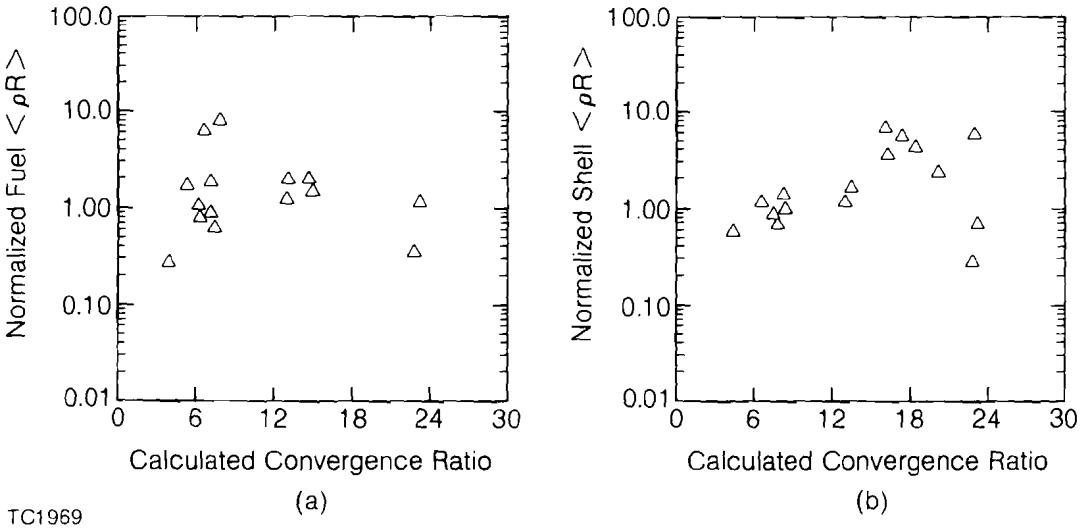

Fig. 25.10
Experimental fuel (a) and shell (b) areal densities, normalized to calculated one-dimensional results, drawn as a function of the calculated convergence ratio.

Further evidence of the existence of nonuniformities is provided by the analysis of K-B microscope images taken from a series of implosion experiments on comparable targets, each illuminated at a different focal position. Since the level of illumination nonuniformity increases with decreasing focal position,[12] experimental agreement with one-dimensional predictions should become poorer as the focal position is

decreased. Comparing the azimuthally averaged film density profile of a K-B microscope image and the corresponding time-integrated profile predicted by *LILAC*, as shown in Fig. 25.11(a), it is possible to determine an average core radius from both the experiment and the simulation. The ratio of the measured core radius to the predicted core radius, versus initial focal position for these targets, is illustrated in Fig. 25.11(b). It can be seen that the agreement between experiment and simulation becomes poorer as the focal position is reduced from 8R (good illumination uniformity) to 2R (poor illumination uniformity).

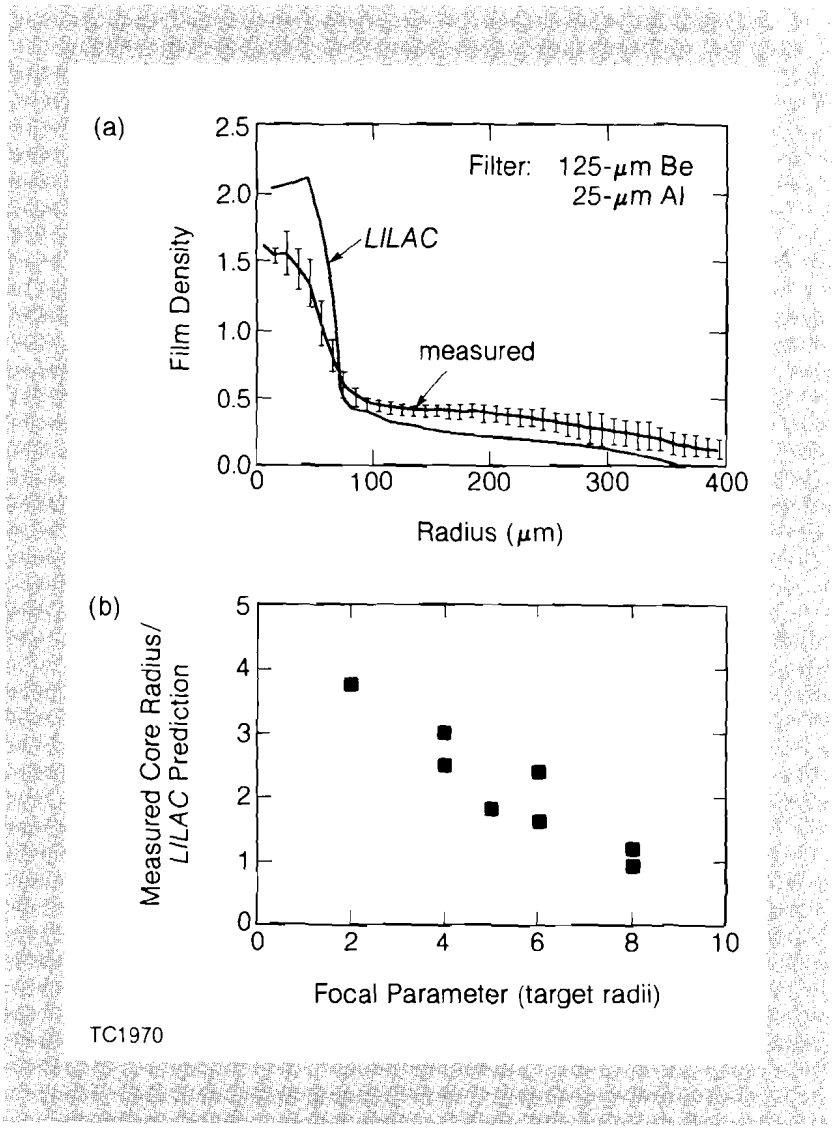

Fig. 25.11
X-ray micrograph profiles: (a) emission comparison between experiment and simulation for shot No. 11309, (b) ratio of averaged core radii (experimental divided by simulated) drawn as a function of initial focal position.

Illumination Nonuniformities

In attempting to understand the effects of the nonuniformities on target performance, it is first necessary to identify the source of the nonuniformities on target. The analysis of the nonuniformities originating from the laser illumination is complex and difficult. Contributions to the illumination nonuniformities can come from several sources, including (1) number of beams, (2) individual beam profile, (3) focal position, (4) energy balance between beams, and (5) beam placement on target.

All of these elements have been incorporated into a computer simulation[12] which decomposes the resulting illumination nonuniformity into its individual spherical harmonics to determine the characteristic spatial wavelengths. Using a typical beam profile from the OMEGA system during the first phase of the 200-XLD campaign, the resultant irradiation pattern was decomposed into its spherical harmonics for various focal positions. The total illumination nonuniformity, as a function of focal position, is shown in Fig. 25.12. The contribution of each individual spherical harmonic (ℓ-mode) to the total nonuniformity for a 6R focus is shown in Fig. 25.13.

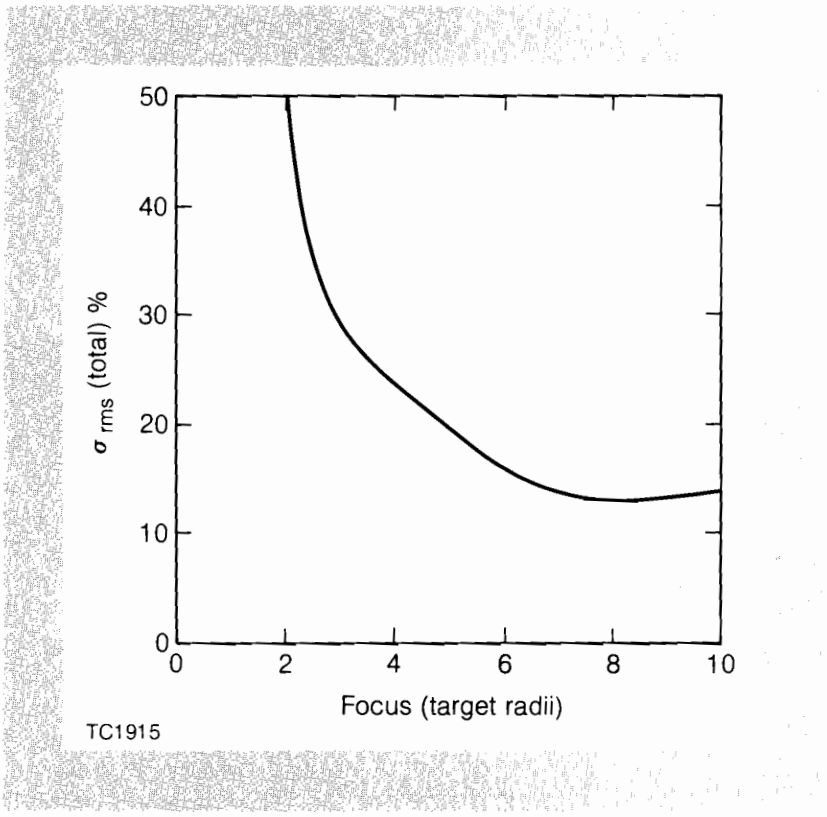

Fig. 25.12
Levels of illumination nonuniformities versus focal position for current OMEGA system.

Once the magnitude and wavelength of the illumination nonuniformity have been identified, they can be incorporated into the two-dimensional hydrodynamics code, *ORCHID*, to determine the effect on performance of an individual target. However, due to limitations in computer resources, it is not possible to simulate the entire illumination nonuniformity. For the nonuniformity spectrum shown in Fig. 25.13, only the ℓ = 2, 4, and 8 contributions, which account for 75% of the total nonuniformity, were used in the simulation. These three modes were combined in phase (producing approximately a 50% peak-to-valley variation characteristic of the calculated nonuniformity), and the resultant nonuniformity was superimposed on normal incident irradiation in the *ORCHID* simulation.

The experiment simulated by *ORCHID* was shot No. 11233, which produced the second-highest neutron yield (1.62×10^{11}) in this implosion series. The *ORCHID* simulation predicted a neutron yield of 5.12×10^{11}, while the one-dimensional simulation gave a yield of

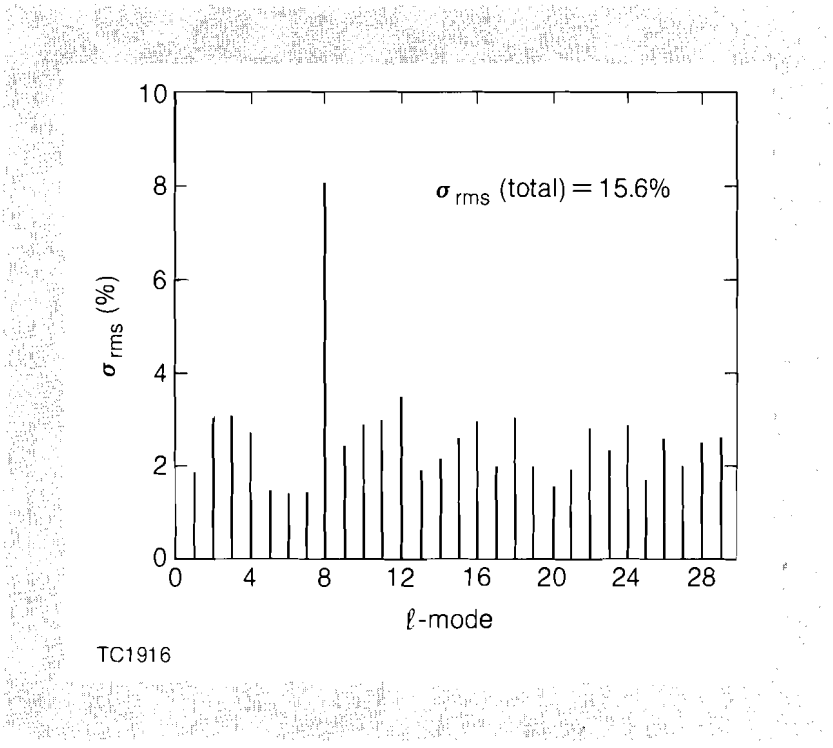

Fig. 25.13
Modal structure of illumination nonuniformity for current OMEGA system at 6R focusing.

2.33×10^{12} neutrons with maximum neutron-averaged fuel and shell areal densities of 2.51×10^{-3} g/cm^2 and 2.75×10^{-3} g/cm^2, respectively. Additional results from the *ORCHID* simulation are shown in Fig. 25.14, with each frame showing the condition of the mesh at different times during the implosion.

The last frame in Fig. 25.14 corresponds to the point in the simulation when the neutron yield equals the total experimental yield. In Fig. 25.15, this frame has been magnified and plots of material density contours, areal density contours, and velocity vectors have been added. From Fig. 25.15(a) it can be seen that the shell-fuel interface has undergone serious deformation, exhibiting a 48% peak-to-valley perturbation. Although the density contours in Fig. 25.15(b) show the same behavior, it is encouraging that the entire fuel region has a density in the range of 0.1 to 0.5 g/cm^3. Areal densities are determined by evaluating the integral of ρdR from the center of the pellet out into the corona, as shown in Fig. 25.15(c). Averaging over the fuel region in this graph gives a value of 1.0 to 1.5×10^{-3} g/cm^2 for the fuel $<\rho R>$. This value is in good agreement with the measured value of $2.13 \times 10^{-3} \pm 3.29 \times 10^{-4}$ g/cm^2 and the one-dimensional result of 1.21×10^{-3} g/cm^2.

The implosion deformations have affected the shell region more seriously. This is especially evident along the polar axis, where – compared with the region along the equator, as shown in Fig. 25.15(b) – significant thinning has occurred. Because of the large variations in density, contributions to the shell $<\rho \Delta R>$ show strong angular dependence. As can be seen in the shell region of Fig. 25.15(c), the integrated values of shell $<\rho \Delta R>$ vary between 5.0×10^{-4} and 3.0×10^{-3} g/cm^2. The average value of 2.12×10^{-3} g/cm^2 is 60%

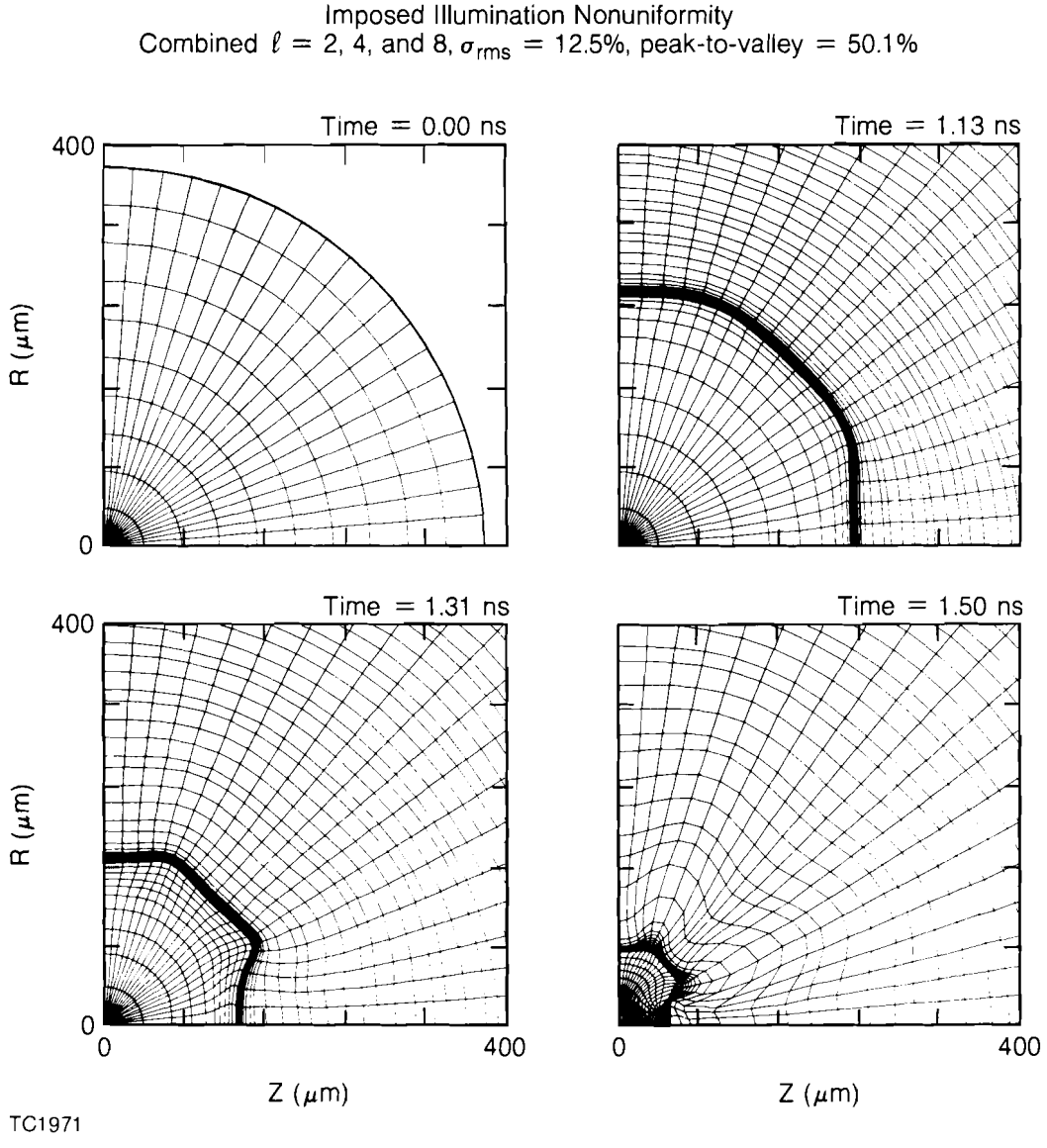

Fig. 25.14
Two-dimensional ORCHID *simulation of shot No. 11233. The imposed illumination nonuniformity was a combined ℓ = 2, 4, and 8 with a total σ_{rms} = 12.5%, corresponding to a 50.1% peak-to-valley perturbation.*

higher than the one-dimensional result of 1.31×10^{-3} g/cm^2. There was no shell $<\rho\Delta R>$ measurement taken for this experiment. The comparison between the one- and two-dimensional results indicates that distorted shells can give higher values of shell $<\rho\Delta R>$ than can the one-dimensional predictions.

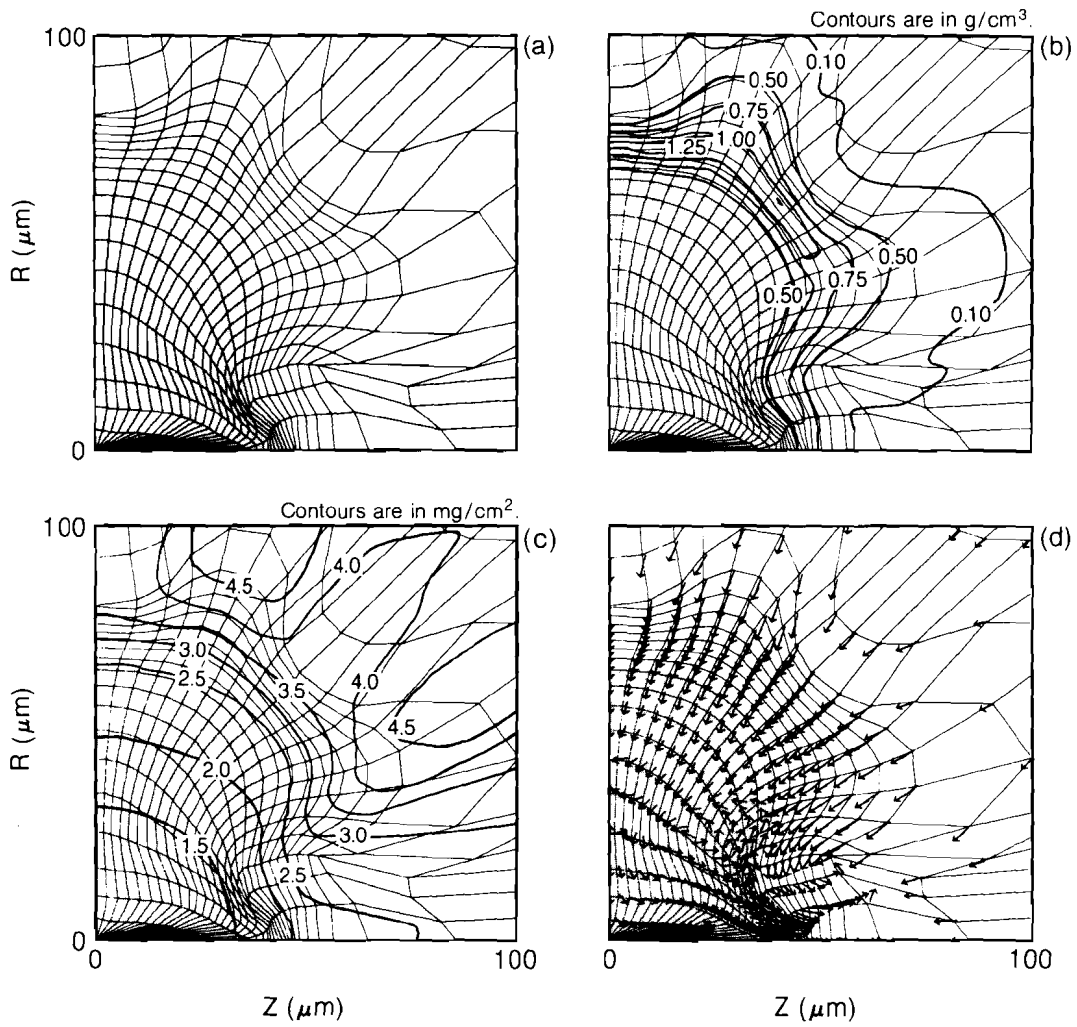

Fig. 25.15
Two-dimensional ORCHID *simulation of shot No. 11233 at 1.50 ns into the simulation:*
(a) grid plot,
(b) material density contours,
(c) areal density contours, and
(d) velocity vector plot.

Finally, in viewing the plot of velocity vectors shown in Fig. 25.15(d), one notes that there is significant fluid motion within the core, especially near the shell-fuel interface along the polar axis. Because the implosion deformations have moved the shell-fuel interface in this area deep into the target, it can be seen that, if mixing processes are present, the swirling fluid motion will transport high-Z impurities from the shell right into the center of the target. The presence of these impurities will seriously affect the core temperature and will possibly quench the burn. Future work on mixing (atomic, chunk, etc.) is needed to determine its effect on overall target performance.

Conclusion

There appears to be agreement between experiment and one-dimensional simulations up to a time prior to maximum compression. After this point in the experiment, however, comparisons between the

experiment and one-dimensional simulations show declining agreement as the predicted convergence ratio increases. The mechanism for this behavior is not yet understood but is probably dominated by nonuniformities imposed on the target during the implosion. Two-dimensional simulations have been carried out with the applied levels of nonuniformities predicted for the OMEGA system and have shown less degradation in target performance than that obtained between experiments and one-dimensional simulations. The two-dimensional work has indicated, however, the need for studying the effects of the glass shell mixing in with the fuel. The severe shell distortions caused by the implosion nonuniformities allow mixing processes (atomic, chunk, etc.) to be able to introduce high-Z impurities deep within the hot fuel core, which would seriously degrade the burn. To what extent the mixing processes are able to affect target performance is dependent on the shape and magnitude of the deformations. Future experiments, therefore, will begin to reproduce increasingly larger percentages of one-dimensional predictions, as problems with illumination uniformity on the OMEGA system are identified and corrected.

ACKNOWLEDGMENT

This work was supported by the U.S. Department of Energy Office of Inertial Fusion under agreement No. DE-FC08-85DP40200 and by the Laser Fusion Feasibility Project at the Laboratory for Laser Energetics, which has the following sponsors: Empire State Electric Energy Research Corporation, General Electric Company, New York State Energy Research and Development Authority, Ontario Hydro, Southern California Edison Company, and the University of Rochester. Such support does not imply endorsement of the content by any of the above parties.

REFERENCES

1. S. Kacenjar, S. Skupsky, A. Entenberg, L. Goldman, and M. Richardson, *Phys. Rev. Lett.* **49**, 463 (1982).
2. E. M. Campbell, W. M. Ploeger, P. H. Lee, and S. M. Lane, *Appl. Phys. Lett.* **36**, 965 (1980).
3. H. Brysk, *Plasma Phys.* **15**, 611 (1973).
4. M. C. Richardson, R. S. Marjoribanks, S. A. Letzring, J. M. Forsyth, and D. M. Villeneuve, *IEEE J. Quantum Electron.* **19**, 1861 (1983).
5. University of Rochester, LLE Report 16 (1976).
6. B. I. Bennett, J. D. Johnson, G. I. Kerley, and G. T. Rood, Los Alamos National Laboratory Report LA-7130 (1978).
7. R. C. Malone, R. L. McCrory, and R. L. Morse, *Phys. Rev. Lett.* **34**, 721 (1975).
8. W. F. Huebner, A. L. Merts, N. H. Magee, and M. F. Argo, Los Alamos National Laboratory Report LA-6760-M (1977).
9. M. Born and E. Wolf, *Principles of Optics* (Pergamon, New York, 1975), p. 123.
10. P. W. McKenty and C. P. Verdon, LLE Theory Group Report No. 15 (1985).
11. LLE Review **24**, 61 (1985).
12. S. Skupsky and K. Lee, *J. Appl. Phys.* **54**, 3662 (1983).

2.B Computerized, Wide-Bandwidth, Multichannel, Soft X-Ray Diode Spectrometer for High-Density-Plasma Diagnosis

The analysis of transient, high-density plasmas such as those produced by high-power lasers and pulsed-power systems often demand a precise, quantitative characterization of the emitted soft x rays. In many cases, such a characterization provides a reliable estimate of the total, radiated x-ray flux, and this has important implications for the radiation and electron thermal transport within the plasma. It critically affects our understanding of the mechanisms responsible for energy absorption, wave propagation, and hydrodynamic instabilities in the plasma. In high-density plasmas these processes occur on a nanosecond time scale. Monitoring the x-ray flux requires a calibrated, broadband, soft x-ray (100- to 2000-eV) spectrometer having a signal bandwidth sufficient to resolve subnanosecond-emission features.

There are, in principle, two architectural approaches to satisfying this requirement for subnanosecond-resolution, broadband, soft x-ray spectrometry on high-density experiments. In many respects they are complementary. The first approach, implemented on several major high-density-plasma facilities, involves using several calibrated x-ray diodes[1] separately filtered for different bands of the soft x-ray region by the incorporation of either K-edge, L-edge, or M-edge filters or specific bandpass x-ray mirrors coated with reflective multilayer structures.[2] The stability of simple metal cathodes used in the x-ray diodes has been studied in detail.[3,4] With a few exceptions, the calibration stability of most metal cathodes has been found to be constant over long time periods (several months) under the typical conditions for these types of experiments, which necessitate frequent vacuum cycling and occasional exposure to oxygen, air, and other elements. With two exceptions,[5,6] the majority of x-ray diodes used in these investigations have response times of several nanoseconds or longer. A spectrometer incorporating diodes having subnanosecond time resolution significantly increases the complexity of the overall system. The diodes themselves must be impedance matched to maintain the signal integrity, and a GHz signal detection system must be used. The fastest commercially available single-pulse oscillographic systems have detection bandwidths of ~1 GHz.[7]

An alternative method of time-resolved, broadband, soft x-ray spectrometry with much greater (≈ 10-ps) temporal resolution is through the incorporation of an x-ray streak camera[8] with an x-ray energy filter system, such as a set of K-edge, L-edge, and M-edge filters[9] or an array of multilayer mirrors,[10] or with a weak x-ray dispersive element such as a freestanding grating.[11,12] The advantage of the latter system is the availability of greater spectral resolution ($\lambda/\Delta\lambda$ up to 100). In addition, systems incorporating streak cameras having soft x-ray photocathodes, usually utilizing thin layers of materials such as Al, Ag, CsI, etc., deposited on 1000-Å plastic foils, and transmissive dispersive optics are difficult to absolutely calibrate, and the calibration stability is less than that of simple metallic x-ray diodes.

Thus, these two approaches are complementary. While a multichannel x-ray diode system provides the greatest calibration stability, a streak camera with dispersive optics[10] has greater spectral and temporal resolution.

At LLE we have recently incorporated both approaches to soft x-ray spectrometry on the OMEGA laser target irradiation facility. A broad array of x-ray diagnostics is now deployed on this facility, including high-resolution x-ray crystal and XUV grating spectroscopy, multichannel hard x-ray (1- to 300-keV) spectrometry, time-resolved x-ray crystal spectroscopy, pinhole camera and microscopic x-ray imaging, and time-resolved streak imaging.

This report describes in detail a multichannel (four-channel), ultrafast (> 1-GHz), soft x-ray diode spectrometer recently deployed jointly by LANL and LLE on the OMEGA target irradiation facility. Signals from these calibrated detectors, which incorporate various thin-film filters to discriminate between different x-ray spectral regions, are recorded on a computerized multichannel digital oscillographic system having an overall bandwidth in excess of 3 GHz.

Multichannel GHz X-Ray Diode Spectrometer

Filtered x-ray photodiode spectrometers have been employed in the ICF community since the early to mid-1970s.[13,14] During this period different photocathode materials were tested, including Si, Al, C, V, Fe, and Cu. In these tests Al showed superior stability and response for channels below 800 eV.[2] The detectors were monitored by standard oscilloscopes.

The X-Ray Photodiodes

The MINIFLEX detector (originally developed by LANL for use on the eight-beam, HELIOS, high-power, CO_2 laser irradiation facility) is built around four identical soft x-ray photodiodes. It is patterned after the seven-channel MULTIFLEX detector used on HELIOS from 1979 to 1983.[4] The principal components of each diode are shown in Fig. 25.16. Each diode is composed of a 50-mesh/inch anode positioned some 1.25 μm in front of a micropolished (dry-diamond-machined) aluminum cathode with an active area of 1.5 cm^2. Experience demonstrates superior long-term stability of micropolished aluminum photocathodes over rough-finished aluminum photocathodes, with some loss of sensitivity for the micropolished cathodes.[16] These aluminum photocathodes cover a nominal sensitivity range from about 60 eV to over 2 keV.[4]

The photocathode is electrically and mechanically attached to a modified vacuum-feedthrough RF connector. Both are positioned inside a vacuum-compatible cavity that also supports the anode and provides the vacuum interface.

The electrical response characteristics of each diode have been measured using picosecond time-domain reflectometry (using a Tektronix S-52 pulse generator and a Tektronix S-6 sampling module in a Tektronix 7S12 time-domain reflectometer). Each diode displayed a

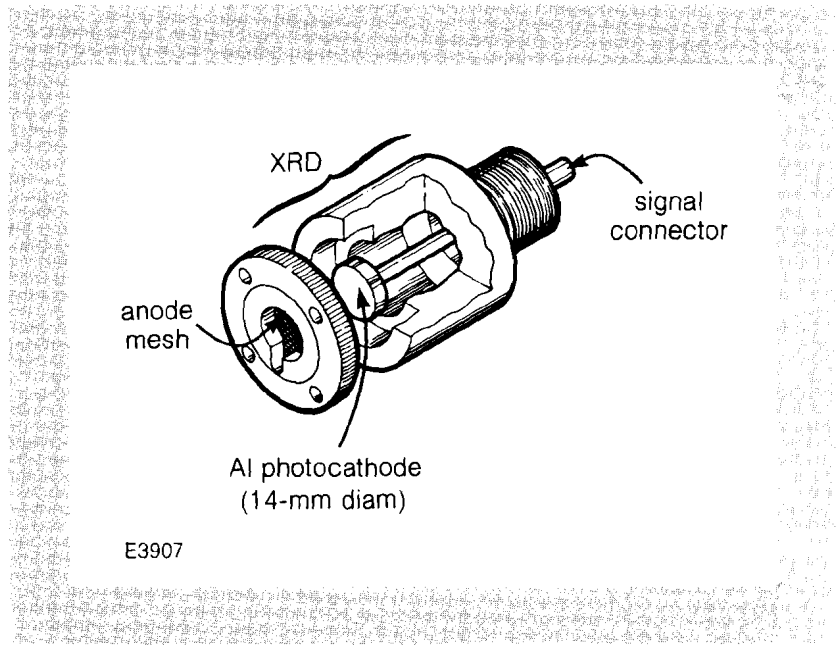

Fig. 25.16
Details of the soft x-ray diode used in the x-ray spectrometer.

nominal response bandwidth of 1.7 GHz. The overall diode sensitivity is dependent on the intrinsic photocathode response, the filter transmission function, and the attenuation of the gold-mesh attenuators. The latter was measured using alpha particles and a surface-barrier spectrometer. *In situ* it was compared with identically filtered but unattenuated channels. The sensitivity of the Al photocathodes was determined from detailed measurements made with dc x-ray sources and calibrated proportional-counter detection.[17] The filter transmission functions were determined from tabulated transmission data and accurate mass and thickness measurements of the individual foils.

The convolution of these three functions then provides an overall sensitivity function for each diode. Typical response functions for a set of four x-ray diode channels used in subkilovolt x-ray emission measurements of laser-produced plasmas are shown in Fig. 25.17.

The X-Ray Diode Detector Assembly

Four x-ray diodes are assembled into an array to form the detector assembly. The x-ray diodes are mounted in a Kel-F[17] plate, which serves as the rear cover for the evacuated, stainless-steel detector housing and provides electrical isolation for the negatively biased diodes. This detector head consists of four individual channels each comprising the x-ray attenuator mesh, the filter stack, a sweeper magnet and collimator tube, and the x-ray diode as shown in Fig. 25.18. Sweeper magnets help inhibit charged particles from entering the diode. In principle, the long time of flight of the charged particles compared to that of the x rays should delay any background. The detector assembly incorporates the four diodes into a single, small-diameter head that attaches to the OMEGA target chamber via a 1.5-m, evacuated flight tube and a gate valve. The flight tube and detector head are evacuated to target-chamber vacuum ($\sim 4\times10^{-6}$ Torr). The gate valve and vacuum interconnects allow intershot modification of filter values of individual channels without perturbation to the rest of the system.

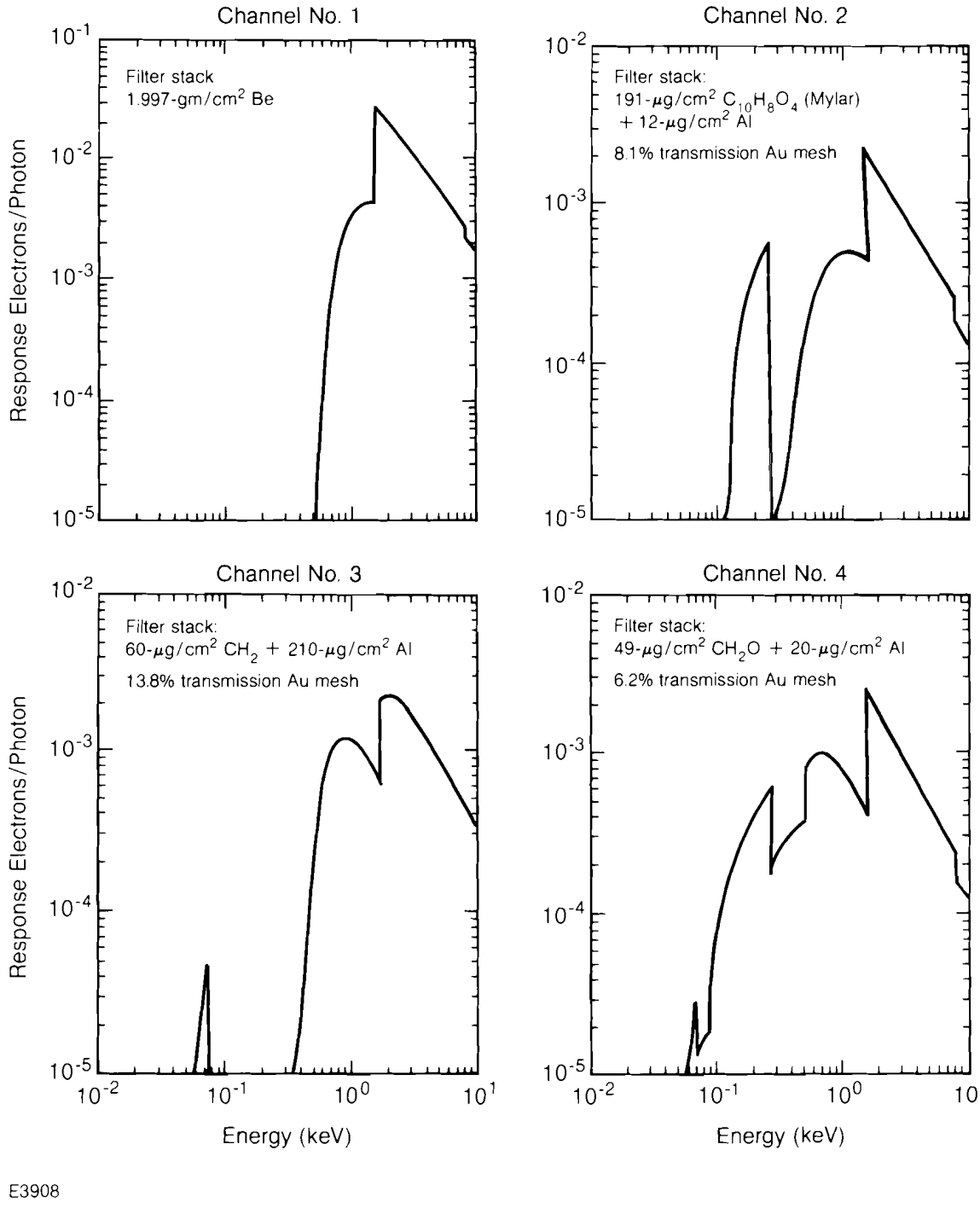

Fig. 25.17
Detailed response curves for the four diodes used in the x-ray spectrometer. These are a convolution of the Al photocathode sensitivity, the filter transmission function, and the attenuation of the anode and the attenuator.

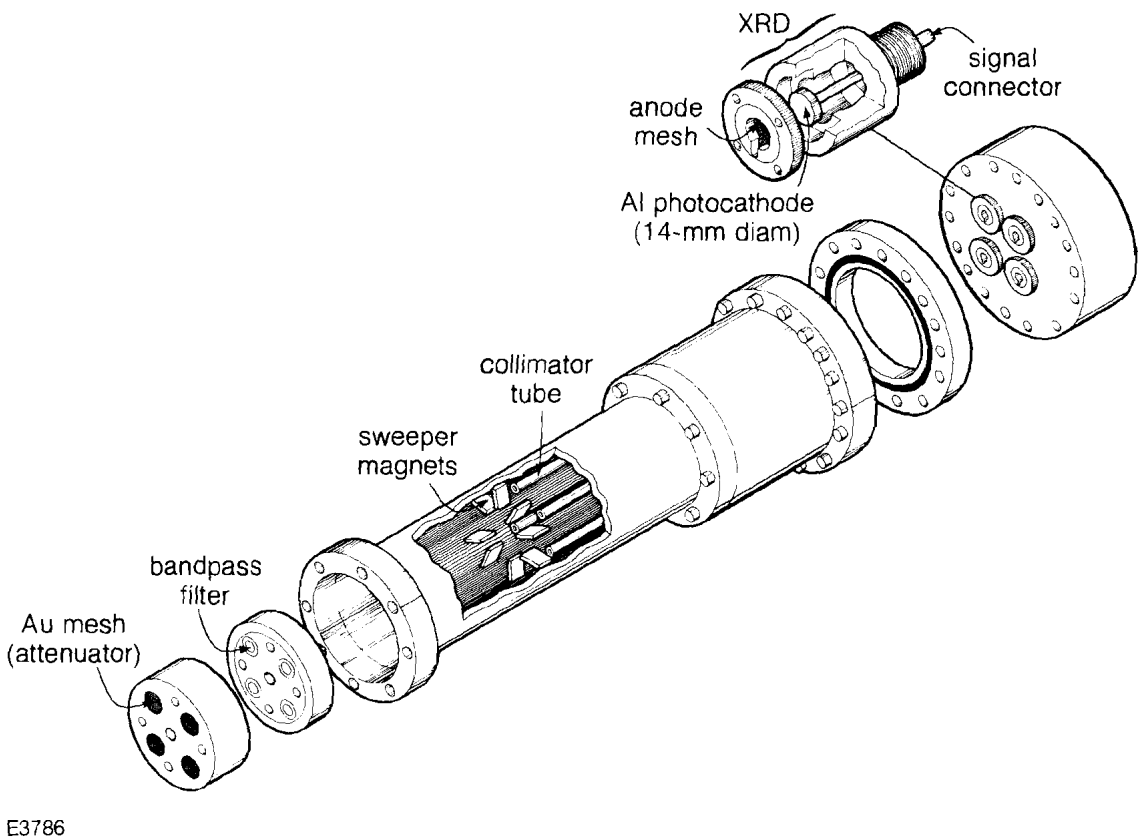

Fig. 25.18
Configuration of the four-detector array in the soft x-ray spectrometer housing.

Signal Recovery

The signal acquisition system used with this x-ray diode spectrometer is based on four Lockheed-modified Tektronix LM7912A transient digitizers. These digital oscilloscopes have been modified[17] to exploit the generic bandwidth of their type 7910 cathode ray tubes. This modification resulted in the designation change from Tektronix R7912 to Lockheed/Tektronix LM7912A. The LM7912A transient digitizer has a bandwidth of 3.5 GHz at the −3dB point, less than 5% undershoot and overshoot, with a 12-bit output (2 mV/bit). It operates under CAMAC control via the Tektronix 7912DPO bus interface. The signal from each x-ray diode is fed via 3 m of RG-214 coaxial cable to a high-speed biasing capacitor, which is connected through 1 m of 50-ohm, semirigid coaxial cable to each of the digital oscilloscopes (see Fig. 25.19). High-bandwidth signal attenuators are optionally inserted into the semirigid leg of the system, as each LM7912A offers only fixed vertical amplification. The LM7912As and their CAMAC crate and controller, as well as timing-control hardware and an on-board calibration pulser, are positioned some 3 m from target center inside an EMI-shielded rack.

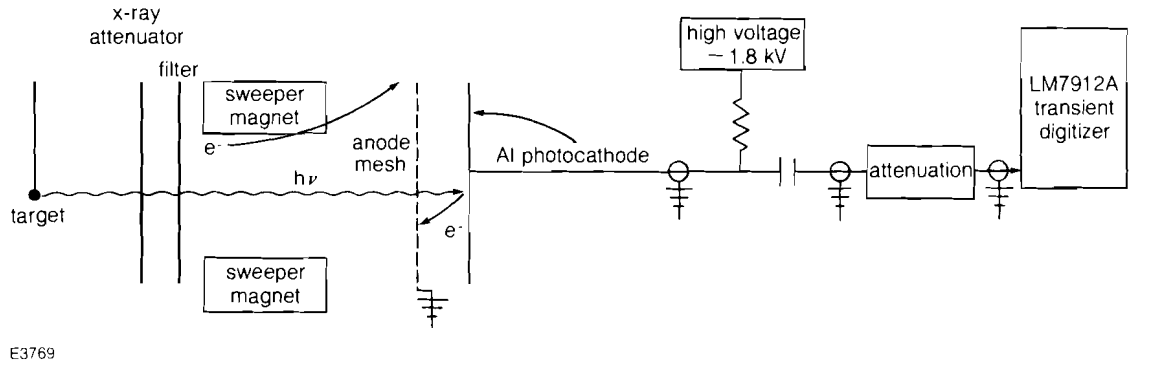

Fig. 25.19
Schematic of the signal acquisition details of each soft x-ray diode.

In order to calibrate the bandwidth response of the system, we substituted a Tektronix S-52 70-ps rise-time pulser in place of the x-ray diode in each acquisition arm. We then acquired traces of this fast-rise pulse using the acquisition system in standard calibration mode (i.e., normal acquisition sequence, with a generated trigger and signal). As shown in Fig. 25.20, the measured 10%–90% rise time of this 200-mV, 70-ps rise-time input pulse was observed as a 200-mV, 130-ps rise-time pulse. Thus, we determined that each acquisition arm performs at a nominal 2.7-GHz bandwidth response at the −3dB point.

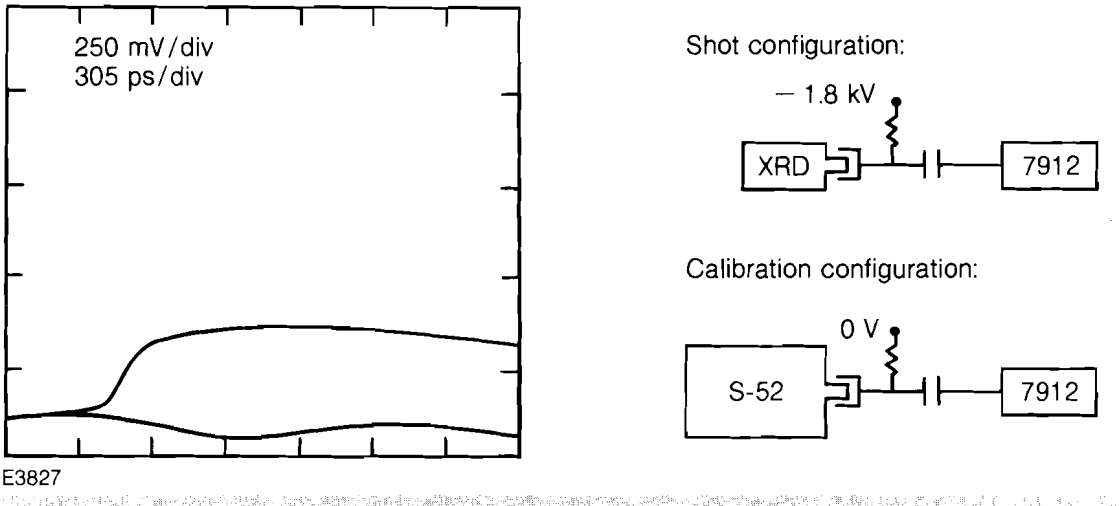

Fig. 25.20
To measure bandwidth response of the acquisition arm, the x-ray diode is replaced by a Tektronix S-52 70-ps, 10-mV pulser. The LM7912A transient digitizer outputs a 130-ps rise-time pulse. This test includes all cables and electrical components for each of the four acquisition arms of the system. As shown, a bandwidth of 2.66 GHz at the −3dB point is confirmed.

Data Recovery

The four LM7912A transient digitizers are all controlled over a Tektronix CP bus, which connects via a Tektronix 7912DPO controller to a fiber-optical-linked CAMAC serial highway. The CAMAC crate and DPO bus are housed along with the LM7912As in the EMI-shielded rack, while the fiber-optic link leads down through the concrete target-bay floor to the OMEGA target diagnostics processor, a DEC PDP 11/23+ operated under RSX-11M. This system is outlined in detail in Fig. 25.21, which shows a schematic of the overall architecture of the transient digitizer acquisition system. The OMEGA target diagnostics processor interconnects into the OMEGA laser system computer network via DECNET. Since many of the OMEGA target diagnostic systems operate under CAMAC, a modular, parameter-driven software scheduling system is used under which individual FORTRAN routines are controlled separately. Modules have been written that initialize and arm the LM7912A transient digitizers, acquire base-line data just prior to each shot, rearm for the event, acquire and archive the shot data, and display and perform preliminary data reduction. These operations are done automatically. Alteration of the vertical amplification of the LM7912A digitizer is facilitated by an attenuation selection. The system may be disabled, when desired, via a menu-driven, parameter-configured operator interface. This interface is common to all of the OMEGA computer-controlled target-diagnostic systems.

Fig. 25.21
Schematic of the signal acquisition and control system of the four-channel, 3-GHz, digital oscilloscope system.

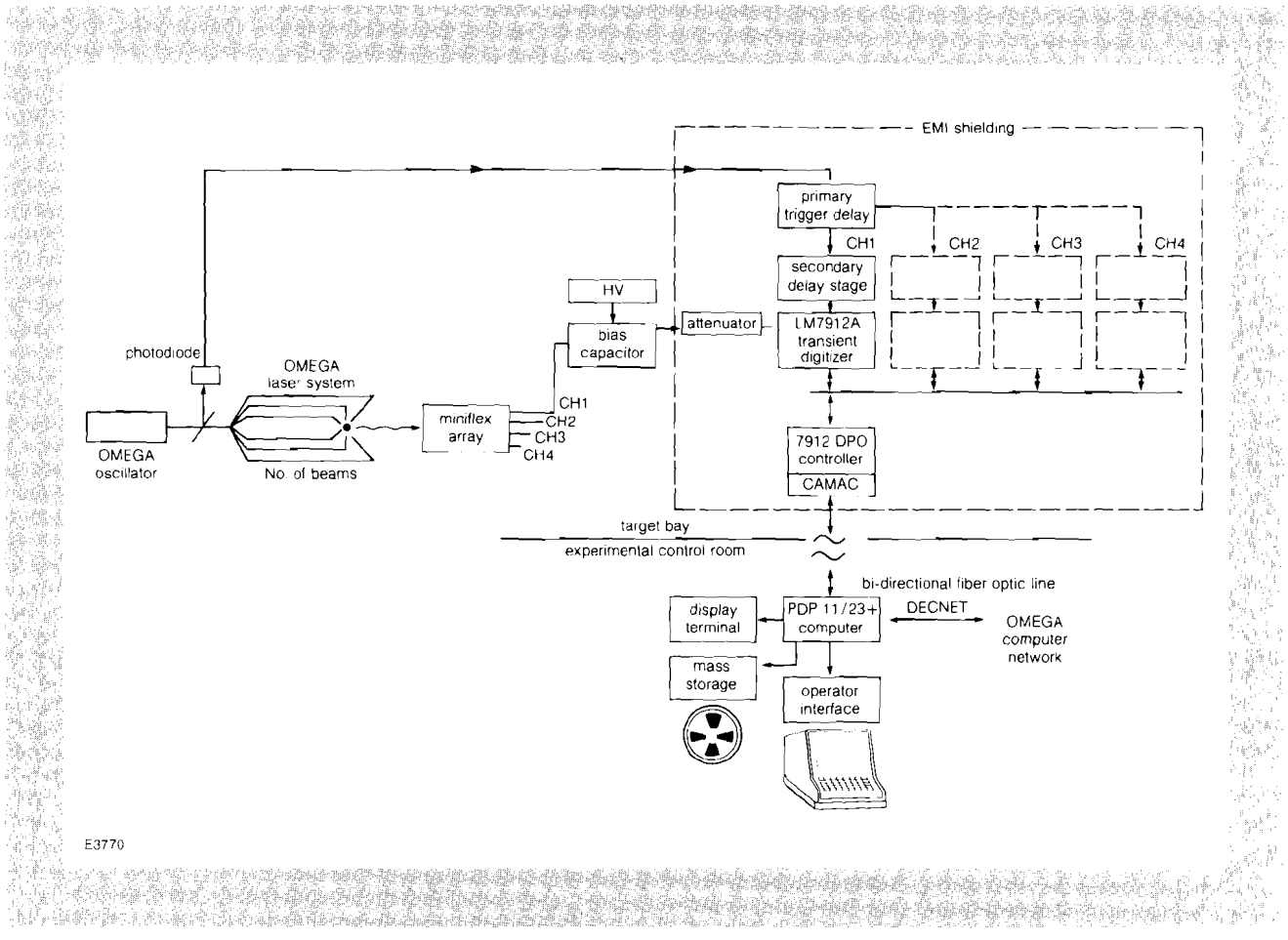

Initial synchronization of the data-acquisition cycle to the timing sequence of the OMEGA shot-diagnostic acquisition system is done through the central computer system, while final synchronization of the data acquisition to the shot is accomplished with a hard-wired timing signal derived from a fast photodiode situated at the front end of the OMEGA laser chain. This photodiode signal is transmitted on a separate HELIAX cable to the EMI-shielded acquisition system and is then run through several delay stages before triggering each separate LM7912A digitizer in synchronism. On the fastest time-base setting used, the acquisition window for each LM7912A digitizer is only 2 ns wide. Synchronization accuracies are better than 100 ps. Synchronization of the triggering of the digitizers is accomplished by substituting a signal from a photodiode mounted on the OMEGA target chamber for each of the x-ray diode signals. The substitute diode samples a lower-power laser pulse propagated from the oscillator through the OMEGA laser system, which serves as a timing mark to synchronize the triggering of the transient digitizers to the laser target interaction. Once each digitizer channel is synchronized to this signal, an offset delay is added to each digitizer trigger-input line to account for the additional x-ray time of flight from the target to the x-ray diode detector array. This system, therefore, ensures minimal (less than 50-ps) triggering jitter in the signal acquisition of the four digitizers.

During each shot cycle, after being automatically armed for a single sweep, the LM7912As are triggered by the photodiode monitoring the laser pulse. The writing beam of the LM7912A encodes the trace on a 512 by 512 diode array in real time. The diode array is then recharged by a reading beam scanning the array over the next 85 ms. These data are stored in on-board memory, and each LM7912A awaits recovery of the data by the controlling software routines. Two files are being written for each OMEGA target shot, one for base-line data and one for event data. Each file carries a system header, followed by four subfiles containing channel data (each from a system parameter file) and that channel's data set. Following the shot, preliminary reduction is performed under full automatic control. Scaling and correction of the data is made for each channel, using previously determined calibration data for that channel. The signal duration (FWHM), peak voltage, and integrated charge are calculated from the digitized signal and base-line record. The base-line and event curves are then displayed on a video screen as a corrected plot with channel parameters and reduced data under the DEC REGIS graphics protocol. A hard copy of the data is created as well. The data files for a particular shot are then transmitted over the OMEGA data network for archiving, along with all other data files for that shot.

Soft X-Ray Measurements on Laser-Produced Plasmas

The soft x-ray diode spectrometer has been used in several experimental investigations on the 24-beam UV OMEGA laser system. Here we discuss interpretation of the time- and energy-resolved data acquired during two experimental programs. Both of these experiments used the soft x-ray diode spectrometer in the configuration described earlier. The only variation between them lies with the different electrical attenuation values ahead of the digitizers to accommodate the particular x-ray fluences germane to each experiment.

X-Ray Conversion Studies

The first[18] of these experiments was a joint LLE-LANL investigation of x-ray conversion in plasmas produced from solid, high-Z (Au)-coated targets at intensities in the range of 10^{13} to 10^{15} W/cm^2. The main purpose of this investigation was a comparison of the x-ray emission spectrum and the x-ray conversion efficiency with the respective findings from previous planar target experiments, and with detailed hydrodynamic computer codes.

As shown in Fig. 25.22, the energy resolution of this spectrometer is obtained by using different filter values for the four channels. The CH_2O/Al filter used in Channel 4 provides information across the 150-eV to 1.5-keV range, CH_2/Al in Channel 3 emphasizes the 700-eV region, Mylar/Al in Channel 2 observes 250 eV and 1 keV, and the Be filter in Channel 1 accepts emission above 800 eV.

The signals from the four channels are then iteratively deconvolved with the spectral response of each detector, to determine the spectral characteristics of the emission.

Fig. 25.22
Typical spectrometer data acquired in experiments on high-Z-coated targets.

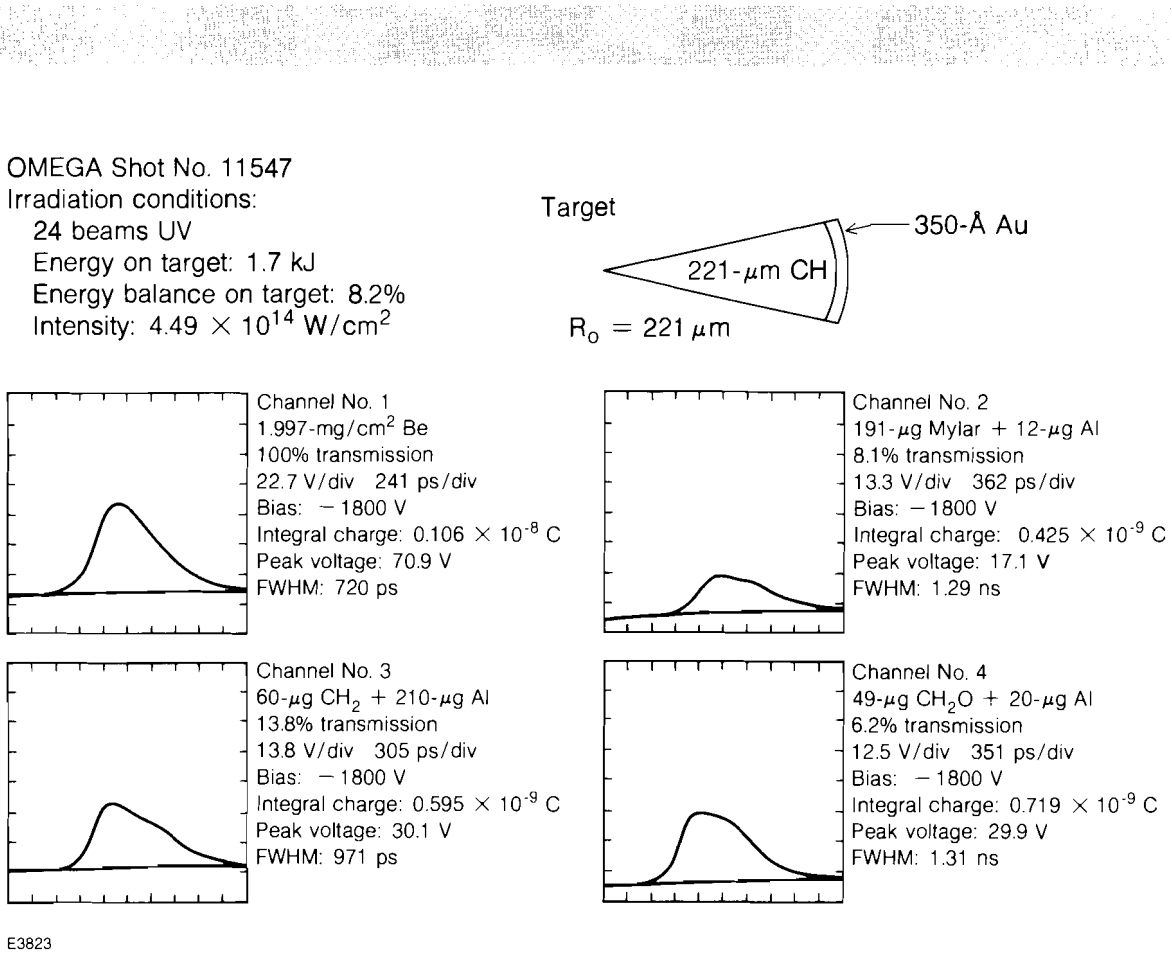

Although the soft x-ray diode spectrometer provides only modest spectral resolution, the high temporal resolution, absolute calibration, and stability of each detector offers reliable, shot-to-shot comparisons of a variety of target parameters. In addition, the ease with which this system can be synchronized to the irradiating laser pulse permits accurate, temporal comparison of the spectral characteristics of the x-ray emission. At present, no other diagnostic system can embody all these characteristics.

Figure 25.22 provides an example for the four-channel output from a single target shot in this series. This particular target was coated with a thin (0.035-μm) layer of gold. The drop in the signal observed in Channels 2–4 results from the penetration into the CH target by the plasma ablation region. Note that in order to calculate the pulse duration (FWHM) and integrated charge one must also plot the base-line response of the system acquired just prior to the event.

Time-Resolved X-Ray Spectrometry of Imploding Laser-Fusion Targets

The soft x-ray diode spectrometer has also been used to acquire data on DT-filled glass-microballoon targets. These experiments[19] were motivated by the question of how symmetric implosions of spherical shell targets could be driven by the 24 351-nm beams of the OMEGA facility. One such series of target shots used large targets with very high initial aspect ratios ($R/\Delta R \sim 200$). Targets of 700- to 800-μm diameters were irradiated at modest intensities ($<2 \times 10^{14}$ W/cm^2). The soft x-ray emission generated in these experiments originates from two sources. This is clearly evident from the set of four-channel x-ray diode data shown in Fig. 25.23. In the initial stages of the interaction, the laser light heats the solid glass shell. X-ray emission results in this case from the hot, dense, coronal plasma surrounding the target. As the shell accelerates inward, it decompresses and the coronal plasma becomes somewhat more tenuous, resulting in a progressive drop in the x-ray emission. Then, as the shell stagnates near the target center, the temperature of the shell is heated, producing a second burst in emission. Deconvolution of the signal from each of these detectors can thus provide valuable information on the coronal conditions during the implosion, on the x-ray emission at peak compression, and on the implosion time. For example, in the data shown in Fig. 25.23, the implosion time of the target can be deduced from the temporal separation (about 700 ps) of the two peaks in x-ray emission.

Summary

We have described in detail the four-channel soft x-ray diode spectrometer activated on the OMEGA irradiation facility for laser-fusion and high-density plasma physics experiments. This instrument is now providing useful spectral, as well as calibrated, soft x-ray emission rate data from different target experiments.

The present instrument provides time-resolved ($\approx$ 160-ps) data of x-ray emission produced by nanosecond laser beams. However, the current system bandwidth is limited by the signal bandwidth of the x-ray diodes. Anticipated future improvements include the development of diode assemblies having a bandwidth greater than the signal bandwidth

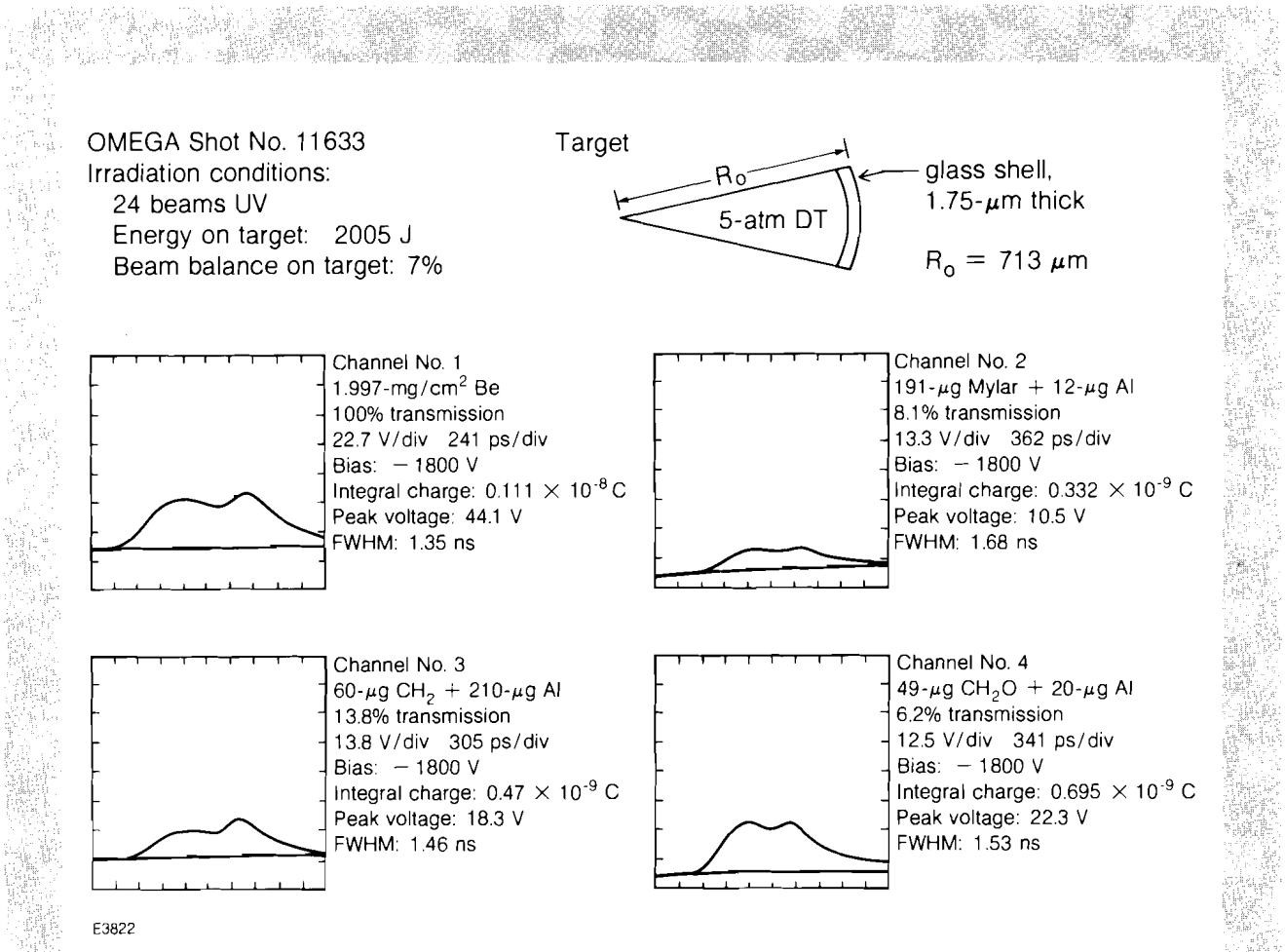

Fig. 25.23
Typical spectrometer data recorded on laser implosion experiments with large initial-aspect-ratio targets imploded at modest (< 2×10^{14} W/cm^2) irradiance.

of the recording digitizers. Such a development would permit the detection of x-ray emission with a time resolution of 100 ps.

The four-channel diode system described here uses foil filters for spectral resolution. These filters permit only a coarse interpretation of the x-ray spectrum. Future improvements would include the addition of more diode channels and the use of multilayer x-ray optical components to provide higher-resolution spectral discrimination.

ACKNOWLEDGMENT

This work was supported by the U.S. Department of Energy Office of Inertial Fusion under agreement No. DE-FC08-85DP40200 and by the Laser Fusion Feasibility Project at the Laboratory for Laser Energetics, which has the following sponsors: Empire State Electric Energy Research Corporation, General Electric Company, New York State Energy Research and Development Authority, Ontario Hydro, Southern California Edison Company, and the University of Rochester. Such support does not imply endorsement of the content by any of the above parties.

REFERENCES

1. For a comprehensive review of the characteristics of soft x-ray detectors, see: R. H. Day, in *Proceedings of the NATO Advanced Study Institute on High-Density Plasma Diagnostics, Pascali, Italy, 1983* (to be published).
2. A recent detailed review of the properties of x-ray mirrors employing multilayer coatings is given by T. Barbee, in *Applications of Thin-Film Multilayered Structures to Figured X-Ray Optics* (SPIE, Bellingham, WA, 1985), Vol. 563, p. 2.
3. B. L. Henke, J. A. Smith, and D. T. Attwood, *J. Appl. Phys.* **48**, 1852 (1977).
4. R. H. Day, P. Lee, E. B. Soloman, and D. J. Nagel, *J. Appl. Phys.* **52**, 6960 (1981).
5. H. N. Kornblum and V. W. Slivinsky, *Rev. Sci. Instrum.* **49**, 1204 (1978).
6. R. H. Day, R. Hackaday, S. P. Ameduri, and E. W. Bennett, *Bull. Am. Phys. Soc.* **25**, 962 (1980),
7. For example, Tektronix 7104 1-GHz oscilloscope.
8. For reviews of current developments on x-ray streak cameras see *High-Speed Photography* (SPIE, Bellingham, WA, 1976–1984).
9. R. S. Marjoribanks, M. C. Richardson, J. Delettrez, S. Letzring, W. Seka, and D. M. Villeneuve, *Opt. Commun.* **44**, 113 (1982).
10. G. L. Stradling *et al.*, *Proceedings of the Topical Conference on Low Energy X-Ray Diagnostics* (AIP Conference Proceedings 75) (AIP, New York, 1981), p. 292.
11. A. M. Hawryluk *et al.*, *Proceedings of the Topical Conference on Low Energy X-Ray Diagnostics* (AIP Conference Proceedings 75), edited by D. T. Attwood and R. L. Henke (AIP, New York, 1981), p. 286.
12. M. C. Richardson, R. S. Marjoribanks, S. A. Letzring, J. M. Forsyth, and D. M. Villeneuve, *IEEE J. Quantum Electron.* **19**, 1861 (1983).
13. J. L. Gaines, H. N. Kornblum, and V. M. Slivinsky, LLNL Report UCRL-75987A (1974).
14. R. H. Day, *Bull. Am. Phys. Soc.* **22**, 1196 (1977); E. J. T. Burns, *Adv. X-Ray Anal.* **18**, 117 (1974).
15. R. L. Carlson *et al.*, *IEEE J. Quantum Electron.* **17**, 1662 (1981).
16. KelF, proprietary product of Minnesota Mining and Manufacturing Company.
17. This modification was implemented by Lockheed Research Laboratories, Palo Alto, CA, under contract to LANL.
18. P. D. Goldstone, S. R. Goldman, J. A. Cobble, A. Hauer, G. Stradling, W. C. Mead, M. C. Richardson, R. S. Marjoribanks, G. Pien, O. Barnouin, and B. Yaakobi, *Bull. Am. Phys. Soc.* **30**, 1364 (1985).

19. M. C. Richardson, P. McKenty, F. Marshall, C. P. Verdon, J. M. Soures, R. L. McCrory, O. Barnouin, J. Delettrez, L. Goldman, R. L. Hutchison, P. Jaanimagi, R. Keck, T. Kessler, H. Kim, S. Letzring, D. Roback, W. Seka, S. Skupsky, and B. Yaakobi, *Laser Interaction and Related Plasma Phenomena*, edited by H. Hora and G. Miley (Plenum Press, New York, to be published), Vol 7.

Section 3
ADVANCED TECHNOLOGY DEVELOPMENTS

3.A Ion-Exchange Strengthening of Nd-Doped Phosphate Laser Glass

Recent advances in high-repetition-rate and high-average-power (HAP) laser systems have put increasing demands on the thermal-loading capabilities of solid-state laser materials. In addition to the material's thermal properties, mechanical and optical limitations must also be identified if a reliable, high-performance system is to be maintained. After considerable effort in materials research at LLE and elsewhere, the physical limitations of various solid-state laser materials become better understood. This article describes specific efforts to increase the thermal-shock resistance of a commercially available, Nd-doped phosphate laser glass. Improvements in this physical property permit a glass to be pumped at levels that may previously have led to its fracture, resulting in a capability for higher-average output powers.

A recently completed HAP laser system at LLE, which serves as a high-repetition-rate source for the in-house damage-testing facility, consists of a phosphate-glass slab through which a beam propagates in a series of zig-zag, total internal reflections. Total internal reflection (TIR) makes efficient use of the entire gain medium. The slab is pumped and cooled on the two TIR sides, which reduces thermal beam distortion often present in alternative geometries. The slab can be operated in the single-pass mode (as an oscillator) or be multi-passed to additionally amplify the oscillator output. These features illustrate how the slab geometry lends itself well to HAP applications.

With renewed interest in HAP systems, emphasis needs to be placed on those properties of glass that make it a better HAP lasing

gain medium. It is essential that the gain of the glass be high if a compact system is to be capable of high average powers. The requirement for a low nonlinear index is not as relevant for these systems, since longer pulses (nanosecond vs picoseconds) are frequently used. However, the issues of chemical compatibility and ease of fabrication become increasingly important. Slabs in most HAP systems utilize continuous cooling provided by a liquid flowing at a relatively high velocity across the pump faces of the glass. The gain medium must be durable, as chemically induced degradation to the precision-polished TIR surfaces would adversely affect output performance.

Fabrication issues become exceedingly important with HAP systems. Slab geometries, in particular, require very tight tolerances. Large polished faces with sharp edges are required to be extremely parallel, flat, and of excellent surface (scratch/dig) quality. Polished Brewster-angle end faces need to be parallel to within arc seconds and of comparable, if not better, quality than the pump faces. For high-performance slabs these stringent fabrication requirements frequently cause high costs and long fabrication times.

The currently most limiting property of glass in HAP applications is its thermal-loading capability, specifically, its relatively low thermal-shock resistance. Byer[1] expresses the average laser power a HAP solid-state gain medium can withstand as the product of the material's thermal-shock resistance and the ratio of plate area to plate thickness. A material's thermal-shock resistance is directly linked to its strength, via the modulus of elasticity, the thermal expansion, and the thermal conductivity. These physical constants determine the stress limit, the fracture stress, at which a material will fail.

The thermal-shock resistance of a material, T_{SH}, is the temperature difference (ΔT) at which the fracture stress (commonly called the tensile yield stress) is reached and failure occurs. This relationship is illustrated in Eq. (1),[2]

$$T_{SH} = \frac{\sigma_f(1 - \mu)k}{\alpha E}, \tag{1}$$

where σ_f is the fracture stress, μ, k, E, and α are the material's Poisson ratio, thermal conductivity, Young's modulus, and linear coefficient of thermal expansion, respectively. Krupke[3] examined the $(1 - \mu)k/\alpha E$ portion of the term as a material figure of merit (FOM). Data compiled for a number of crystalline and noncrystalline materials show that the FOM is much larger for crystals than for glasses. The FOM, coupled with each material's known tensile yield stress, indicates that crystals are several times more thermal shock resistant than glasses. Yet, crystalline materials of high optical quality and homogeneity are considerably more expensive than their glass counterparts and are in some cases simply unavailable in acceptable sizes. Because of these limitations, we have chosen to examine the potential of external treatments in improving the strength of

commercially available high-performance laser glass. Here we confine the discussion to Q-89, a phosphate-composition glass manufactured by Kigre, Inc.[4]

Any external strengthening treatment aims at introducing a compressive surface stress into the glass, in order to increase the stress required to fracture the glass in tension. Marion[5] has shown that by reducing surface and subsurface damage in the form of microcracks (point sources where failure begins), via an acid etch, one can increase the fracture strength of a material. This benefit comes, however, at the expense of the optical surface quality and of the material's thickness, from which ~ 200 μm are removed. Our alternative approach is to chemically treat the surface by way of an ion-exchange process (cracks included), in which the surface becomes stronger through the introduction of a layer of compressive stress to the glass surface. This ion-exchange strengthening can be performed without loss of optical surface quality.

Ion-exchange processing is routinely carried out by the glass industry in strengthening various products. The mechanism involves the exchange of a mobile alkali-ion A^+ that is present throughout the bulk material with a slightly larger ion B^+ of identical valence. The exchange is carried out in a molten-salt bath at an elevated temperature to accelerate the exchange of diffusing ions. The mobile A^+ ions readily diffuse out of the bulk, leaving vacancies behind. The larger B^+ ions migrate from the salt bath into the glass by occupying the small A^+ vacancies. The important feature of this "crowding" mechanism, as outlined by Kistler,[6] is that it is performed at temperatures sufficiently below the strain point of the glass. An optimized treatment schedule prevents structural relaxation from occurring; as a result of the predominance of the larger ions, the surface is "expanded" into compression. A number of factors will control the net compressive stress that results from the process:[7]

- the radius ratio of the exchanging ions
- the degree to which the exchange occurs
- stress relaxation due to structural rearrangement of the surface
- any change in thermal expansion coefficient
- localized densification
- the depth of the compressive layer

Of these factors, the depth of the compressive layer is the most important. That layer can be thought of as a physical barrier that impedes the propagation of cracks. A thick layer will be more resistant to abrasion and thus failure, since any flaw would have to penetrate *past* this depth to initiate fracture.

Considerable work has been done on the strengthening of silicate glass. To our knowledge, the process has not previously been extended to phosphate laser glass. While the basic mechanism remains the same, the composition of the base glass network determines the efficacy of the treatment. Silicates lend themselves well to ion exchange because their network consists of openly spaced

SiO_4 tetrahedra. This open network creates channels through which alkali ions can migrate easily.

The structure of phosphate glass is more complex. Whereas SiO_4 tetrahedra in silicate networks are able to bond to form similar tetrahedra, phosphate glasses are composed of PO_4 tetrahedra, which are limited in that they can only bond to three like structures during network formation.[8] For this reason, Al_2O_3 is frequently added to assist as a network former in a phosphate-glass matrix. This, coupled with relatively large amounts of another network modifier, BaO, leads to a much more closed structure. This tighter matrix impedes the diffusion of alkali ions deep into the glass. Silicate glass systems strengthened via ion exchange obtain, therefore, thicker compressive layers than phosphates.

The diffusion process that controls the exchange mechanism is very sensitive to changes in the exchange bath. Physical variations due to particulates, moisture, ion concentration, and other forms of bath contamination severely decrease the effectiveness of the process. In this work the primary A^+ alkali ion is Li^+, a major constituent in Q-89 in the form of Li_2O. The exchanging B^+ ions are Na^+ and K^+, present in the bath as nitrate salts. Figure 25.24 depicts the ion-

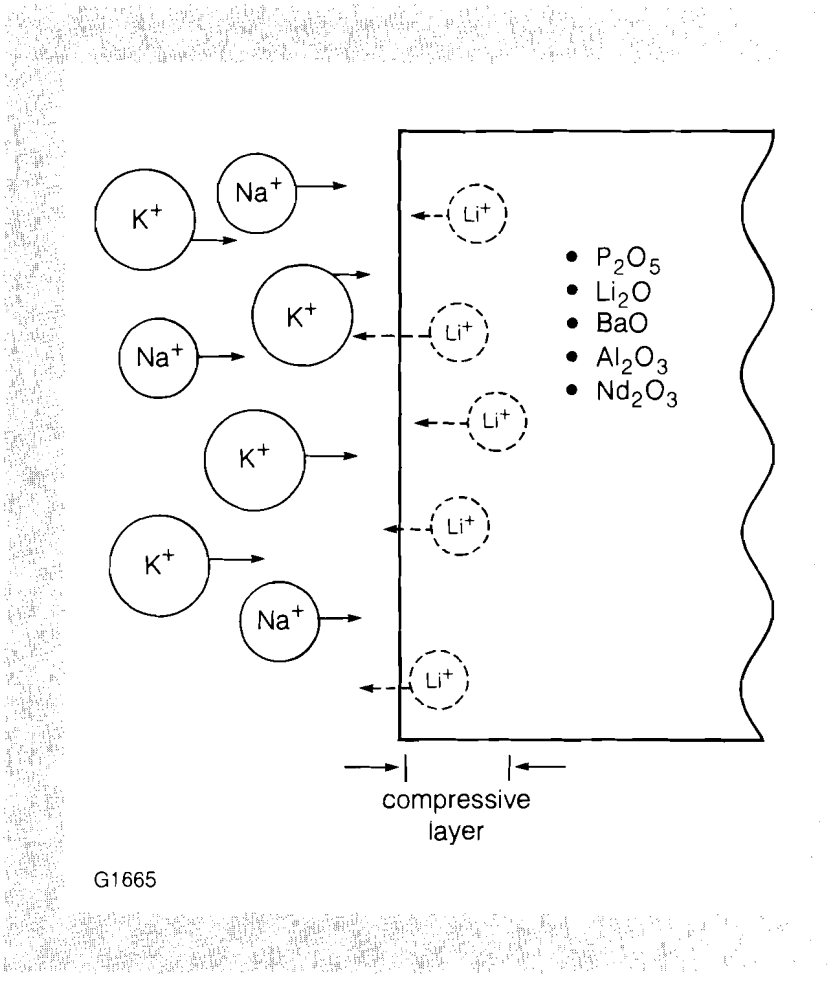

Fig. 25.24
Ion-exchange mechanism in Kigre Q-89. Mobile Li^+ ions diffuse out of the glass, leaving vacancies behind. Na^+ and K^+ ions preferentially diffuse from the bath into the Li^+ vacancies, crowding into the smaller vacancies and creating a compressive layer on the glass surface.

exchange mechanism in Q-89 and lists the other major constituents of this glass. The stoichiometry of the nitrate salts used in the bath is important; a large Na^+/K^+ ratio would be desired since Na^+ is the predominant exchanging ion. However, Na^+ is corrosive, and in applications such as these, where post-treatment surface quality is critical, a tradeoff must be made.

Several experiments have been conducted to examine methods for optimizing the strengthening process. The various test geometries and results are described as follows:

1. Thermal-shock tests

The improved strength through ion-exchange treatment was determined by a series of thermal-shock-resistance tests. Samples of Q-89 were fabricated into right-circular cylinders, 0.63 cm in diameter by 0.63 cm in length with fine-ground surfaces (#400 grit), acid etched in NH_4HF_2 for ~6 min prior to exchange treatment. The cylinders were then evaluated for their thermal-shock resistance through a soak/quench test. Treated cylinders were placed in an oven, raised to a prescribed temperature, and "soaked" at that temperature for ~30 min to guarantee sample-to-sample temperature uniformity. The samples were then removed and plunged into ice water (~5°–7°C). Upon removal from the ice bath, each sample was visually inspected for fracture. If no fracture occurred, the $\Delta T(T_{oven} - T_{water})$ was recorded and the process repeated at a soak temperature increased by +10°C. This continued until all samples had fractured. Results from these tests are shown in Fig. 25.25. Cylinders were treated in the exchange bath for 0, 2, 4, 6, and 10 days. The treatment time [in $(hours)^{1/2}$] is plotted in Fig. 25.25 versus measured

Fig. 25.25
Fivefold increase in thermal shock resistance in cylindrical, Q-89 samples. Excellent statistics (±5%) can be attributed to a clean, contamination-free bath.

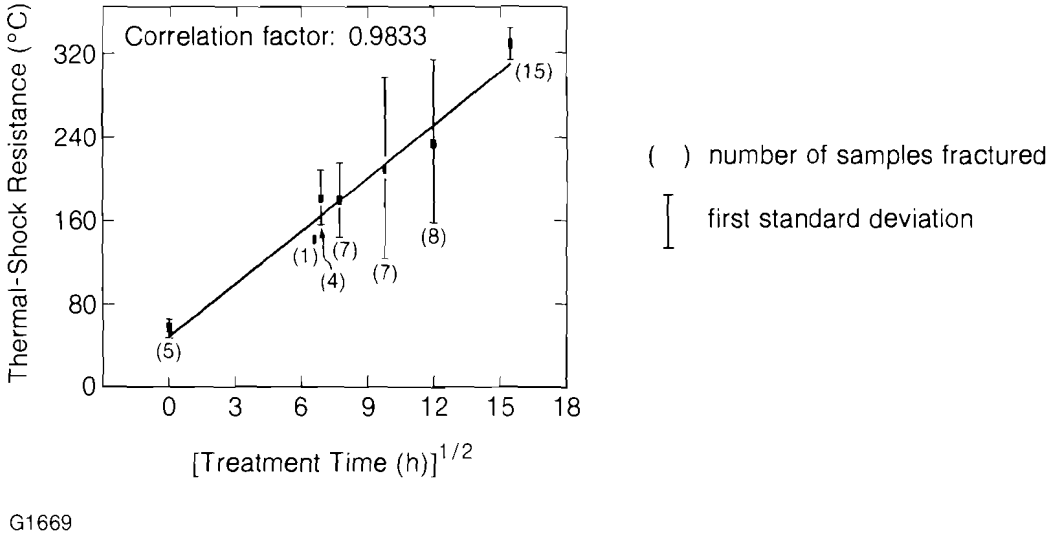

thermal-shock resistance, in °C. The treatment was carried out at an exchange-bath temperature of 320°C, with samples treated statically (no agitation) and removed and rinsed with de-ionized water every other day to remove any residual material buildup on the sample surfaces.

Introduction of a compressive layer through ion exchange resulted in a fivefold increase in thermal-shock resistance. Our thermal-shock test data show extremely small (approximately $\pm 5\%$) standard deviations compared with the 50%–100% variation observed in data acquired through conventional mechanical-fracture techniques.

The widening spread in data for days 1–6 is a result of an increase in the level of bath contaminants. Depletion of diffusing ions and increased moisture content of the treatment bath are believed to have led to a larger standard deviation and poorer sample surface quality. The treatment of 15 samples for ten days in a new, dry bath restored the low standard deviation and improved sample surface quality. Although samples treated longer than ten days were not tested, it is important to note in Fig. 25.25 that we did not yet observe any leveling off in the strength improvement data. Thus, the ultimate levels of strength improvement are not known at this point and deserve further investigation.

Ion penetration depths of approximately 60 μm were measured via electron microprobe analysis.[9] A depth profile for the light, highly mobile Na^+ ion that preferentially diffuses into the glass is shown for a six-day treated sample in Fig. 25.26(a). Similar profiles for one-

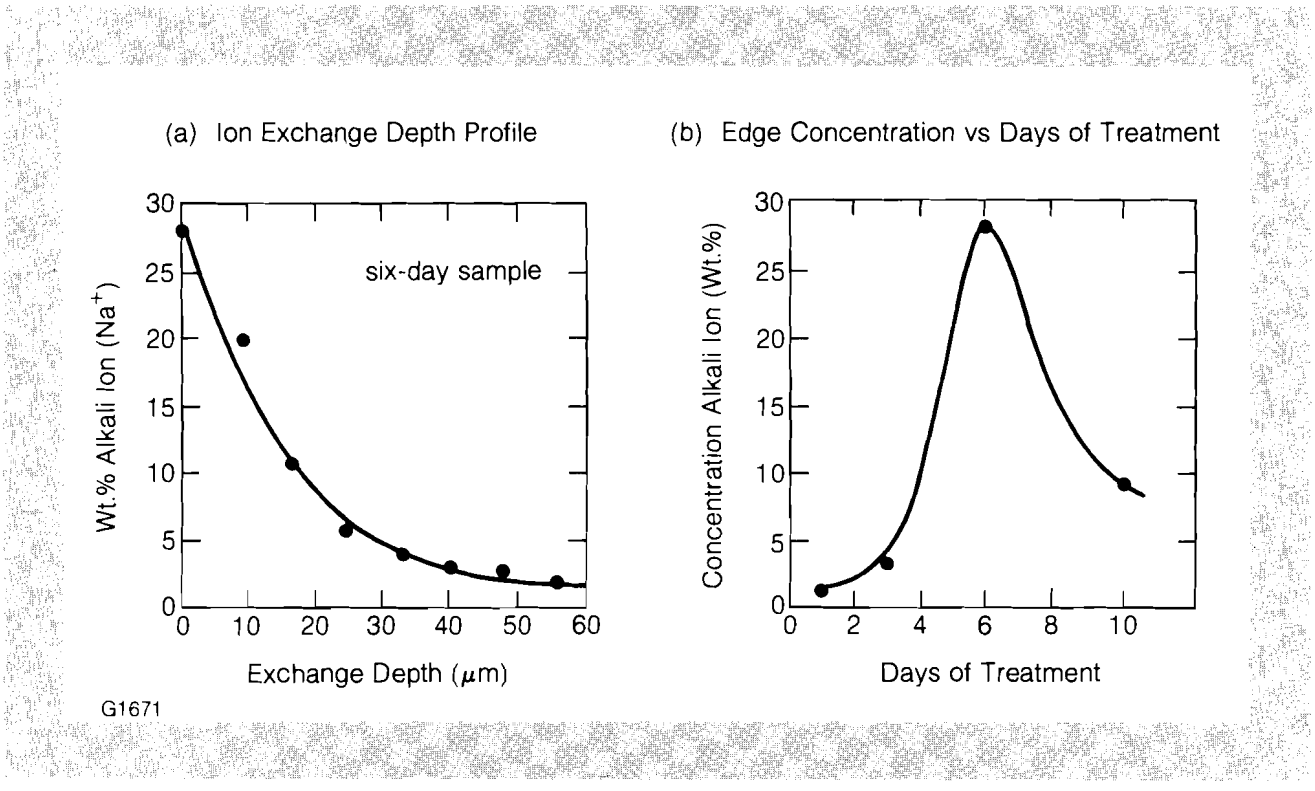

Fig. 25.26
(a) Ion-exchange depth profile for six-day treated sample, as determined by electron microprobe analysis.
(b) Edge profile of alkali (Na^+) ion concentration as a function of treatment time. Rollover after six days may be due to stress relaxation mechanism in glass network, which allows migration of Na^+ ions away from surface and further into the bulk.

through four-day samples showed an alkali-ion dropoff to the detection limit at depths of 35 to 40 μm. However, six- and ten-day samples remained at ~3%–5% levels considerably further into the bulk. This observation is useful in explaining alkali-ion edge concentration data shown in Fig. 25.26(b). Here, we plot the edge concentration of alkali (Na^+) ions as a function of days of treatment. The rollover that occurs after six days may be due to stress-relaxation processes occurring in the glass network at the elevated bath temperature of 320°C. This stress relaxation could allow ions in high concentrations at the material's edge to migrate further into the bulk, thus decreasing the concentration at the edge.

Current work is focused on answering a number of questions relating to the details of the exchange mechanism. Reproducible profiles of light-ion concentrations are difficult to obtain and can be improved by fabricating samples with very clean edges. Supplemental analytical techniques will assist in confirming the details of the ion exchange, specifically in the analysis of the compressive layer.

2. Refractive-index variation in the surface layer

In examining the optical effects of the strengthening process, experiments were designed to investigate the new compressive surface layer. The surface refractive-index variations were measured as a function of days of treatment. A polished half cylinder was measured unstrengthened and then remeasured following additional one-day increments of treatment. These measurements were made on an Abbé refractometer, at λ = 632.8 nm and at a temperature of 22°C. The results of these tests are plotted in Fig. 25.27. The

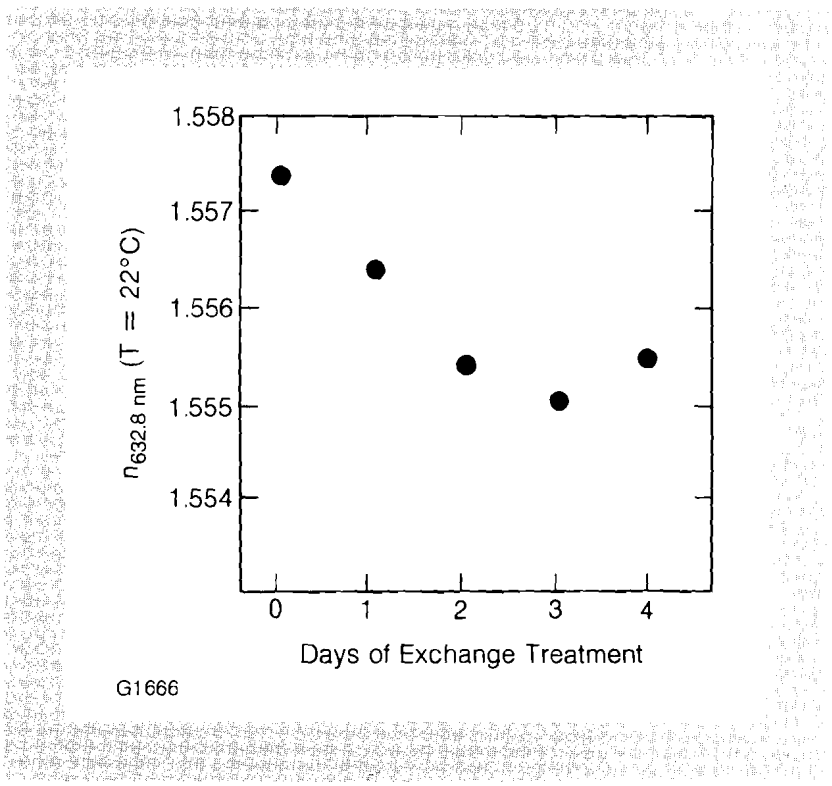

Fig. 25.27
Refractive-index variation in surface layer as a function of days of treatment. Measured index decreases as Li_2O/R_2O ratio decreases.

observed index decrease in the third decimal place is consistent with Kigre bulk-glass data for Q-89, which indicate a decrease in refractive index with decreasing Li_2O/R_2O ratio. This decrease continues to occur in the strengthened layer with additional days of treatment. It is not expected that this small reduction in the surface index causes any deleterious effect on the TIR propagation of the beam through a strengthened slab.

3. TIR transmission tests

This experiment focused on treatment-induced degradation to optically polished surfaces. Thin slabs of Q-89, 15 × 75 × 3 mm, were fabricated for TIR transmission measurements, at λ = 1064 nm and at a glass-air interface. The objective was to examine surface degradation and increased scatter as well as possible limitations to TIR as a function of exchange-treatment time. Measurements on treated slabs were compared with the transmission through an untreated control sample. A YAG (λ = 1064 nm) laser was injected at ~45° (> critical angle, θ_c = 40°) into the slab through a BK-7 prism, which was index-matched to the Q-89 surface, as shown in Fig. 25.28(a). After a series of TIR bounces the beam exited the sample and the total transmission drop was monitored. From this observation the reflectance per bounce was calculated. The result is shown as a solid line in Fig. 25.28(b).

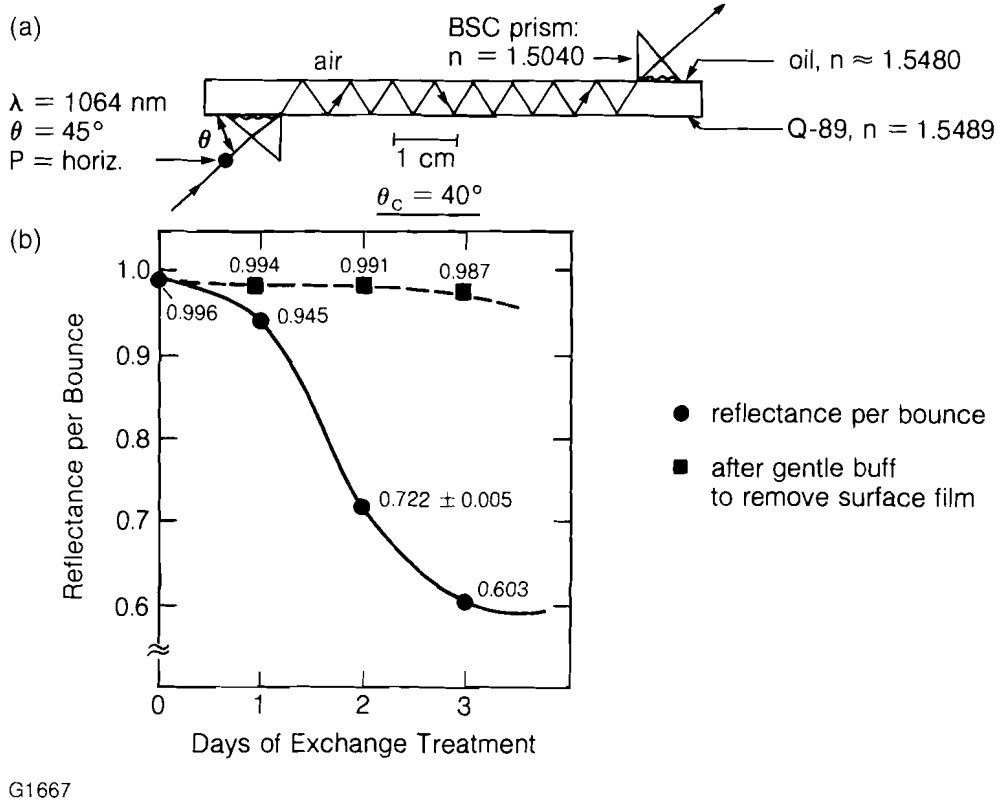

Fig. 25.28
(a) Total internal reflection (TIR) experiment on thin slabs of Q-89 at $\theta = 45°$ and λ = 1064 nm; measurements were made in air. (b) Reflectance per bounce decreases as a function of days of treatment. Gentle buff of treated surface restores TIR reflectance to the >99% level.

Surface films may become apparent after as little as three days of treatment. Visible inspection of the samples after treatment showed a very irregular, mottled film, which gradually worsened with treatment time. This film caused the steady drop in reflectance that was observed as treatment time was lengthened. A gentle buff removing the surface film was found adequate to restore TIR reflectance to the 99% level. Minimal (<0.5 μm for three-day sample) material removal was required to achieve this improvement. This encouraging test was based on a worst-case experiment, due to the use of an old, contaminated salt-bath treatment of that sample. We suspect that the observed surface film is the result of moisture contamination in the bath,[10] which can be eliminated with proper preventive measures.

The details of the process as outlined here support the claim that phosphate laser glass can be strengthened effectively. The demonstration of a fivefold increase in thermal-shock resistance of Q-89 illustrates the potential of this technique. A first step in assessing the impact of the ion-exchange process on the optical surface quality of fabricated parts is completed.

Several issues are unresolved. Work is continuing to address the issues of bath contamination, optical surface degradation due to moisture, the effect of exchange treatment on the interferometric quality of fabricated parts (optical surface deformation due to compressive stress), and the compositional gradients of the compressive-stress layer. Scalability of current results from test-specimen scale to full-sized slab samples is of major importance. Results from these investigations will further enhance the capabilities of high-average-power laser systems with phosphate-glass gain elements.

ACKNOWLEDGMENT

This work was supported by the General Electric Company Advanced Laser Technology Group, Binghamton, NY, under contract No. A25-E-0580BS, the New York State Center for Advanced Optical Technology of the Institute of Optics, and the sponsors of the Laser Fusion Feasibility Project at the Laboratory for Laser Energetics, which has the following sponsors: Empire State Electric Energy Research Corporation, General Electric Company, New York State Energy Research and Development Authority, Ontario Hydro, Southern California Edison Company, and the University of Rochester. Such support does not imply endorsement of the content by any of the above parties.

REFERENCES

1. R. Byer, "Slab Geometry Lasers," presented at International Lasers and E-O Exhibition, Tokyo, Japan, 31 January 1985.
2. W. D. Kingery *et al., Introduction to Ceramics* (Wiley, New York, 1975), p. 823.
3. W. F. Krupke, LLNL Report UCRL-89439 (1983).
4. Kigre, Inc., 5333 Secor Road, Toledo, Ohio 43623
5. J. Marion, LLNL Report UCRL-92680 (1985).
6. S. S. Kistler, *J. Am. Ceram. Soc.* **45**, 59 (1962).
7. S. D. Stookey, in *High Strength Materials: Proceedings of the Second Berkeley International Materials Conference,* edited by V. F. Zackay (Wiley, New York, 1965), p. 669.

8. W. D. Kingery *et al., Introduction to Ceramics* (Wiley, New York, 1975), p. 110.
9. Analysis performed by Xerox Analytical Laboratory, Jos. C. Wilson Center for Technology, Webster, NY.
10. Dr. W. LaCourse, Institute for Glass Science and Engineering, Alfred University, Alfred, NY (private communication).

3.B Short-Pulse Amplification Using Pulse-Compression Techniques

Traditionally, short pulses have been amplified by dye or excimer amplifers. Nd:glass, in spite of its remarkable energy-storage capability, was not utilized because of the difficulty to extract efficiently the stored energy at a high repetition rate. A technique analogous to the one used in the radar field is described, which allows the amplification of short pulses to a level two to three orders of magnitude beyond the state of the art. This technique should make possible the generation of picosecond pulses at the joule level.

As early as 1940, scientists[1-5] working in radar proposed to amplify short pulses, using compression techniques as a way to decrease the peak power in the transmitter tubes while increasing the radar range and resolution. The general approach is shown in Fig. 25.29(a). It uses a linearly chirped pulse with a total frequency modulation ΔF. The pulse, after traversing some dispersive elements, is stretched to a length several times its original value so it can be amplified efficiently without reaching a prohibitive peak power. After amplification, the pulse is broadcast. Its echo is compressed by a matched filter to a pulse width approximately equal to $1/\Delta F$. The final result is a large increase in both radar range and accuracy.

In the laser field, scientists and engineers working in short-pulse amplification have faced the same peak-power limitation in laser amplifier stages.[6] Pulses in the picosecond range can quickly reach relatively high peak intensities in the GW/cm^2 range. At these intensities, nonlinear effects occur that may cause beam wave-front distortion, filamentation, and irreversible damage to components. The net result is that short-pulse amplifiers have to be operated in a small-signal-gain regime far from saturation, leading to unwieldy, inefficient systems working at low repetition rate. Nd:glass amplifiers are a good example. In the absence of nonlinear effects, Nd:glass is capable of amplifying optical pulses up to a fluence of 5 J/cm^2 before saturation occurs, as opposed to 3 mJ/cm^2 for dye amplifiers. For a 1-ps pulse, 5 J/cm^2 corresponds to a power density of 5 TW/cm^2, about one thousand times the limit set by nonlinear effects in glass. This constraint can now be overcome by a technique analogous to short-pulse amplification in radar.

The principle of the amplification is depicted in Fig. 25.29(b). Relatively short, low-energy pulses are delivered by a mode-locked oscillator. Before amplification, they are coupled into a single-mode fiber, where they simultaneously experience self-phase modulation and group velocity dispersion. The self-phase modulation taking place at the early part of the fiber produces sidebands to the laser spectrum, whereas the group velocity dispersion stretches each pulse into a rectangular pulse with a duration several times its initial value.

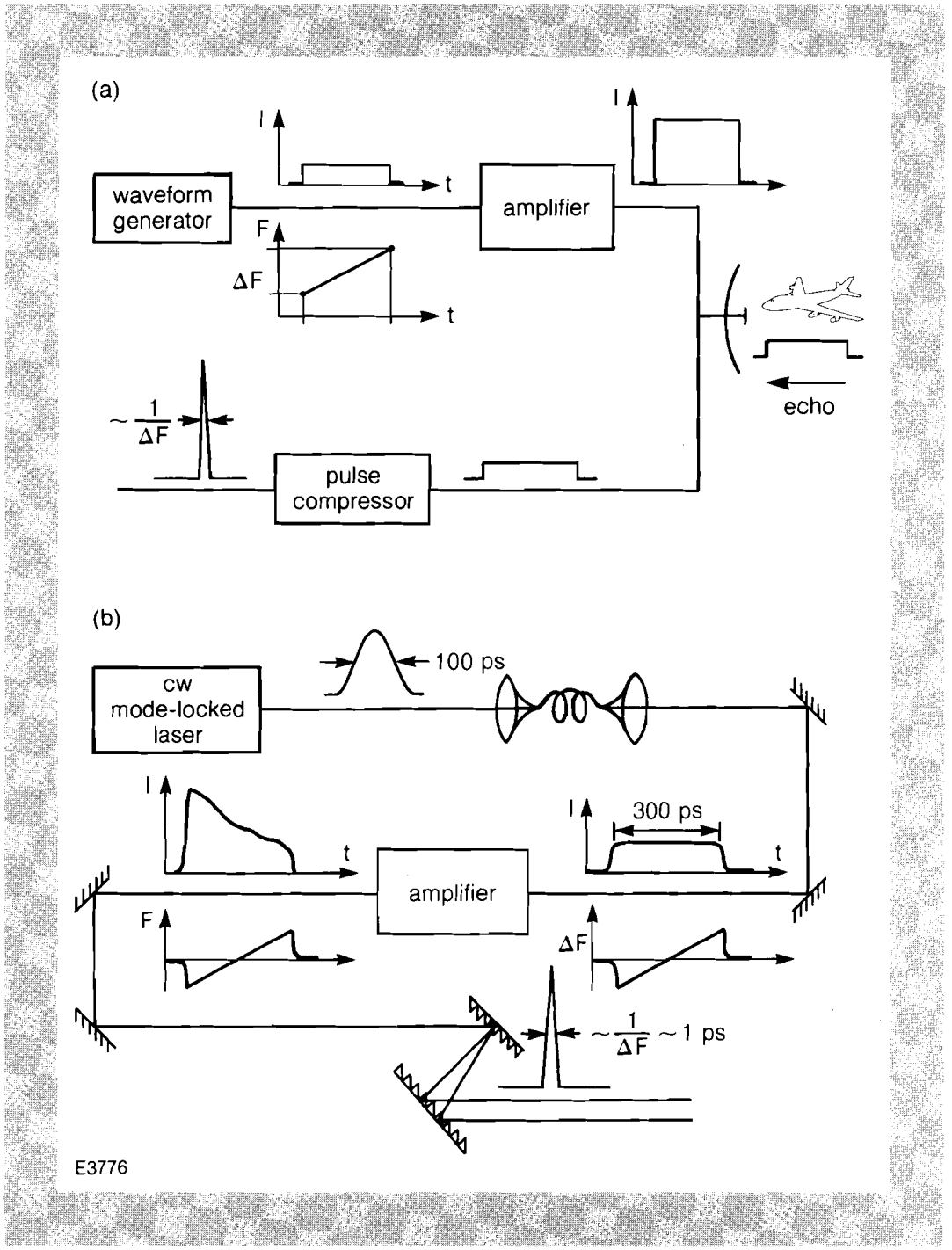

Fig. 25.29
The pulse compression of chirped pulse in radar (top) and its optical analog.

At the fiber output the pulses have a rectangular pulse envelope with a linearly swept carrier frequency.[7] At this point the coded pulses are amplified without fear of undesirable nonlinear effects. The amplifier gain bandwidth has to be broader than the pulse spectrum in order not to limit the pulse spectrum. After amplification, the pulse is compressed in time by a pair of gratings to a value approximately equal to $1/\Delta F$ of the initial value. This short-pulse amplification scheme, using frequency chirping and pulse compression, has recently been demonstrated.[8]

A cw mode-locked Nd:YAG laser is used to produce low-energy, 100-ps optical pulses at a 100-MHz repetition rate. The pulses are injected into a 1.4-km-long single-mode fiber. Due to the combined effect of self-phase modulation and group velocity dispersion, pulses of 200 ps exhibiting a linear chirp are produced at the fiber output (see Fig. 25.30). The linear chirp is spread over 40 Å. The 200-ps pulses are injected into a regenerative amplifier using silicate glass (Kigre Q-246) as the active medium, which exhibits a gain bandwidth of 200 Å. The pulses are injected into the regenerative-amplifier cavity at a repetition rate of 5 Hz by a single Pockels cell. After 40 round trips in the laser cavity, the laser pulses attain an energy of 2 mJ and are cavity dumped by the same Pockels cell. Because of gain saturation the output-pulse amplitude is not rectangular but still exhibits a linear frequency chirp across the pulse. The pulse is subsequently compressed by a set of two gratings to a pulse width of 1.5 ps. The overall grating efficiency is 50%, yielding an output pulse of 1 mJ. Figure 25.31 shows a streak camera trace of the amplified and compressed pulse and a reflection from an etalon.

If we compare this system to other existing systems[9] based on dye lasers amplified by Nd:YAG or excimer lasers, producing millijoule-level pulses of 1 ps at a similar repetition rate, one is struck by the simplicity, compactness, beam quality, and much superior efficiency

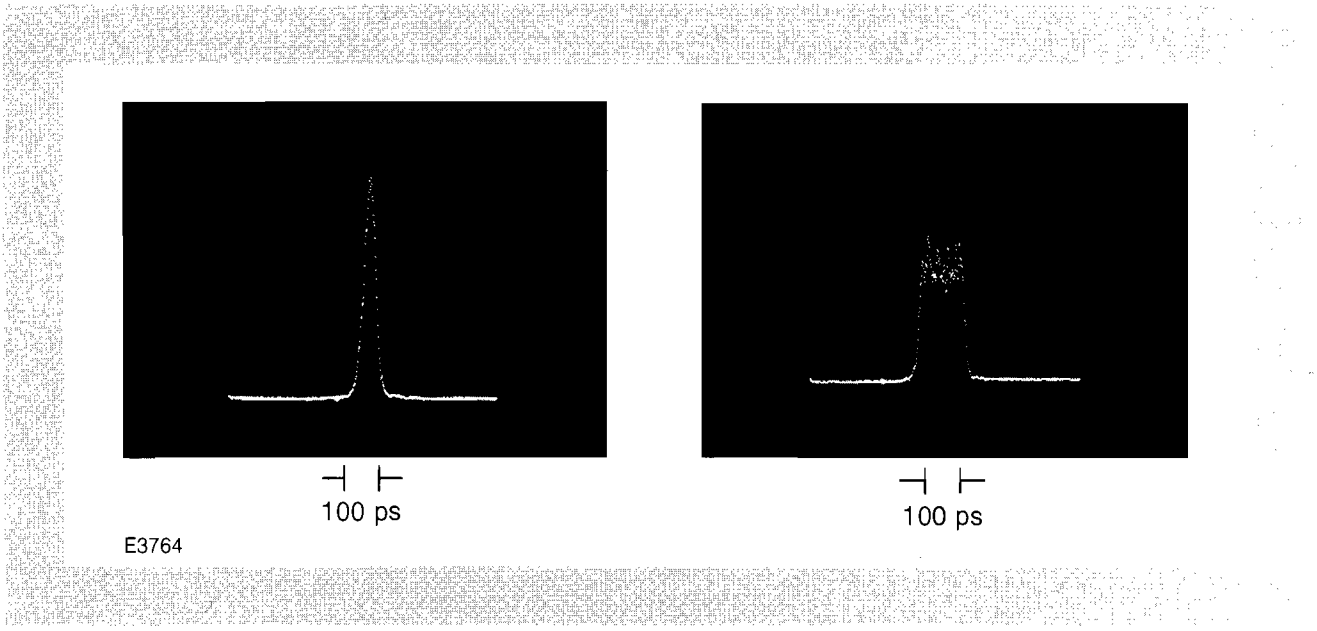

Fig. 25.30
Pulses at the fiber input and output monitored by a streak camera. The pulse has been frequency doubled for detection needs.

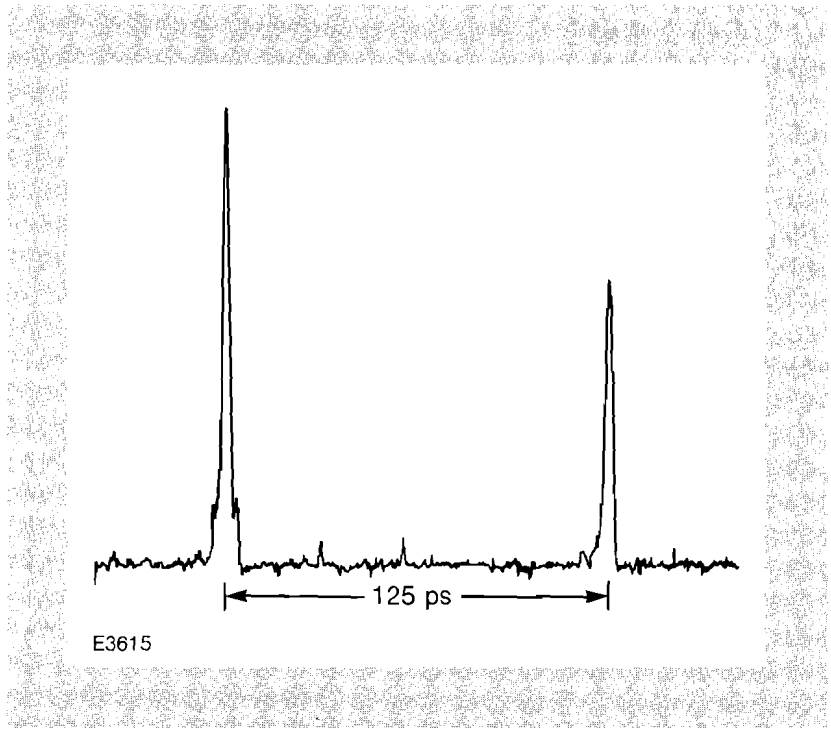

Fig. 25.31
Short pulses after amplification. Because the streak camera has a visible photocathode, the pulse had to be frequency doubled.

of this system. It is worth noting the enormous potential of this concept especially for glass systems – which, unlike dyes, have a large energy-storage capability. Pulses with durations of a few hundred picoseconds are presently amplified from the joule to the kilojoule level, and now, with this technique, femtosecond and picosecond pulses with equivalent energies may be produced. Opportunities arise for sources two to three orders of magnitude brighter than existing ones; conversely, one could produce equivalent brightness with a system that had 10^2 to 10^3 times less energy per pulse. To illustrate the dramatic improvement this technology offers, Fig. 25.32 shows the experimental curve of the energy per pulse as a function of pulse width available on the glass development laser at LLE. We have also plotted the energy available with the pulse compression technique. Curve (a) represents what could be obtained today and curve (b), what could be obtained assuming that nanosecond-to-picosecond compression is possible. The curves (a) and (b) are, of course, parallel to the time axis because the pulse is amplified at constant pulse width. It is the compression that determines the pulse duration.

We have demonstrated that a technique of pulse chirping is able to produce pulses with a brightness two to three orders of magnitude greater than any existing source. Pulses with peak powers of 10^{15} to 10^{16} W can in principle be achieved, opening new possibilities for studying matter under intense irradiation.[10] For the spectroscopist interested in the picosecond time scale, this new system is simpler, more efficient, more compact, less costly, and has sufficient power density to produce white-light continua. Finally, this system makes long-range and high-accuracy radar possible because of the large amount of energy now available in short pulses.

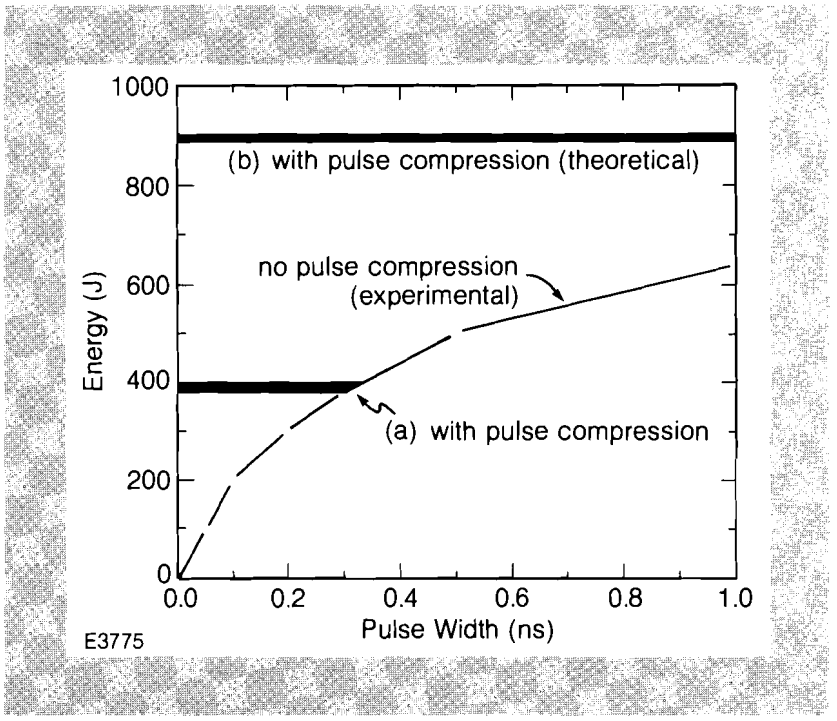

Fig 25.32
Energy obtainable on the glass development laser at LLE as a function of the laser pulsewidth. Note that for the curves (a) and (b), the energy is independent of the final laser pulsewidth since the amplifier sees a constant input pulsewidth.

ACKNOWLEDGMENT

This work was supported by the Laser Fusion Feasibility Project at the Laboratory for Laser Energetics, which has the following sponsors: Empire State Electric Energy Research Corporation, General Electric Company, New York State Energy Research and Development Authority, Ontario Hydro, Southern California Edison Company, and the University of Rochester. Such support does not imply endorsement of the content by any of the above parties.

REFERENCES

1. E. Huttman, German Patent No. 768068 (22 March 1940).
2. W. A. Cauer, German Patent No. 892772 (19 December 1950).
3. D. O. Sproule and H. J. Higle. British Patent No. 604429 (5 July 1948).
4. R. H. Dicke. U.S. Patent No. 2 624 876 (6 January 1953).
5. S. Darlington. U.S. Patent No. 2 678 997 (18 May 1954).
6. For instance see M. M. T. Loy and Y. R. Shen, *IEEE J. Quantum Electron* **9**, 409 (1973) or W. Koechner, *Solid State Laser Engineering* (Springer-Verlag, 1976), p. 592.
7. H. Nakatsuka and D. Grischkowsky, *Opt. Lett.* **6**, 13 (1981).
8. D. Strickland and G. Mourou, *Opt. Commun.* (to be published).
9. For a review of various amplification schemes, see *Picosecond Phenomena III: Proceedings of the Third International Conference on Picosecond Phenomena (1982),* edited by K. B. Eisenthal, R. M. Hochstrasser, W. Kaiser, and A. Laubereau (Springer-Verlag, 1982), pp. 10, 19, and 107.
10. K. Boyer and C. K. Rhodes, *Phys. Rev. Lett.* **54**, 1490 (1985).

Section 4
NATIONAL LASER USERS FACILITY NEWS

National Laser Users Facility (NLUF) activity during the first quarter of FY86 was primarily in three areas: NLUF experiments were conducted on the OMEGA facility; the 1986 NLUF Steering Committee was formulated; and 15 proposals were received for consideration for the 1986–87 funding cycle.

NLUF experiments during this quarter were carried out for **U. Feldman** and **J. Seely** of the Naval Research Laboratory. The experiments, using the UV OMEGA laser at energy levels between 500 and 1600 J, were for characterizing the XUV spectra of Fe, Y, Zr, Nb, Mo, Ru, Rh, Ag, Cd, Sm, Gd, and Eu. The primary objective of this program is to record high resolution ($\Delta\lambda/\lambda < 1000$ spectra) of isoelectronic sequences of interest for possible soft x-ray laser transitions. Rich spectra were observed from all of the elements attempted. Spectra from excited states of F-like and O-like ions were observed in the range of 20 to 300 Å for elements Fe through Cd; interest in the spectra of Sm, Gd, and Eu is stimulated by speculation regarding the possibility of x-ray laser generation on Ni-like ion transitions. The recorded spectra are now being analyzed at the Naval Research Laboratory.

In December 1985, the Department of Energy approved a list of potential members of the next NLUF Steering Committee. The formulation of the Committee and planning for its meeting to consider next year's proposals was under way as of the writing of this report.

In December we received 15 proposals for consideration by the next Steering Committee. The proposed experiments range from fundamental atomic physics to cryogenic fuel implosion.

Proposals for consideration for the FY88 funding cycle are due by 15 December 1986.

For more information regarding proposal guidelines and the resources available at the National Laser Users Facility, please contact:

Manager
National Laser Users Facility
Laboratory for Laser Energetics
University of Rochester
250 East River Road
Rochester, New York 14623-1299
(716) 275-2074

ACKNOWLEDGMENT

This work was supported by the U.S. Department of Energy Office of Inertial Fusion under agreement No. DE-FC08-85DP40200.

PUBLICATIONS AND CONFERENCE PRESENTATIONS

Publications

K. E. Meyer and G. A. Mourou, "Two-Dimensional E-Field Mapping with Subpicosecond Resolution," in *Picosecond Electronics and Optoelectronics,* edited by G. A. Mourou, D. M. Bloom, and C. H. Lee (Springer-Verlag, Berlin, Heidelberg, New York, Tokyo, 1985), pp. 46–49; S. Williamson and G. A. Mourou, "Picosecond Electro-Electron Optic Oscilloscope," *ibid.*, pp. 58–61; K. E. Meyer, D. R. Dykaar, and G. A. Mourou, "Characterization of TEGFETs and MESFETs Using the Electro-Optic Sampling Technique," *ibid.*, pp. 54–57; C. J. Kryzak, K. E. Meyer, and G. A. Mourou, "Transmission Line Designs with a Measured Step Response of 3 ps per Centimeter," *ibid.*, pp. 244–248; D. R. Dykaar, T. Y. Hsiang, and G. A. Mourou, "Development of a Picosecond Cryo-Sampler Using Electro-Optic Techniques," *ibid.*, pp 249–252.

U. Feldman, J. F. Seeley, M. C. Richardson, W. E. Behring, and S. Goldsmith, "Transitions of the Type 2s-2p in Fluorine-Like and Oxygen-Like As, Se, Br, and Rb^{x}," *J. Opt. Soc. Am. B* **2**, 886–890 (1985).

P. Horn, P. Braunlich, and A. Schmid, "Photoacoustic Determination of Three-Photon Absorption Cross Sections in Thallium Halides at 1.06 μm," *J. Opt. Soc. Am. B* **2**, 1095–1099 (1985).

D. P. Butler and T. Y. Hsiang, "Transient Relaxation of the Normal State Resistance of Tin Microstrips in the Presence of Current Bias," *J. Low Temp. Phys.* **61**, 69–78 (1985).

M. D. J. Burgess, R. Dragila, B. Luther-Davies, K. A. Nugent, A. J. Perry, G. J. Tallents, M. C. Richardson, and R. S. Craxton, "Characterization of Plasmas Produced by a Laser Line Focus," *J. Phys Rev. A* **32**, 2899–2908 (1985).

D. Strickland and G. Mourou, "Compression of Amplified Chirped Pulses," *Opt. Commun.* **55**, 447–449 (1985).

J. F. Seely, C. M. Brown, U. Feldman, M. Richardson, B. Yaakobi, and W. E. Behring, "Evidence for Lasing on the 182-Å Transition of CVI in a Radiation-Cooled Plasma," *Opt. Commun.* **54**, 289–294 (1985).

R. L. McCrory and J. M. Soures, "Laser Fusion Experiments at the University of Rochester," *Nucl. Fusion* **25**, 1367–1372 (1985).

Forthcoming Publications

S. D. Jacobs, "Liquid Crystal Devices for Laser Systems," to be published in the *Journal of Fusion Energy.*

S. Williamson, G. Mourou, and J. C. M. Li, "Time-Resolved Laser-Induced Phase Transformation in Aluminum," to be published in the *Proceedings of MRS Symposium on Energy Beam-Solid Interactions and Transient Thermal Processing.*

B. Yaakobi, R. D. Frankel, J. M. Forsyth, and J. M. Soures, "Laser-Generated X-Ray Source for Time-Resolved Biological and Material Structure Studies," to be published in the *Proceedings of a Symposium on New Methods in X-Ray Absorption, Scattering, and Diffraction.*

The following papers are to be published in the *Proceedings of the Workshop on Physics of Laser Fusion*, Vancouver, B.C., June 1985 (*Canadian Journal of Physics*):

A. Simon, "Raman Scattering."

J. Delettrez, "Thermal Electron Transport in Direct-Drive ICF."

L. M. Goldman, "The Use of Laser Harmonic Spectroscopy as a Target Diagnostic."

W. R. Donaldson and G. A Mourou, "Improved Contacts on Intrinsic Silicon for High Voltage Photoconductive Switching," to be published in the *Proceedings of the Fifth IEEE Pulsed Power Conference*, Arlington, VA, June 1985.

The following papers are to be published in the *Proceedings of the SPIE 29th Annual International Technical Symposium on Optical and Electro-Optic Engineering,* San Diego, CA, August 1985:

G. G. Gregory, S. A. Letzring, M. C. Richardson, and C. D. Kiikka, "High Time-Space Resolved Photography of Laser Imploded Fusion Targets."

P. A. Jaanimagi, B. L. Henke, and M. C. Richardson, "An Absolutely Calibrated Time-Resolving X-Ray Spectrometer."

M. C. Richardson, G. G. Gregory, S. A. Letzring, R. S. Marjoribanks, B. Yaakobi, B. L. Henke, P. A. Jaanimagi, and A. Hauer, "Time-Resolved X-Ray Spectrographic Instrumentation for Laser Fusion and X-Ray Laser Studies."

R. L. McCrory, "Inertial Confinement Fusion (ICF)," to be published in *Physics Today*, January 1986.

R. Epstein, S. Skupsky, and J. Delettrez, "Effects of Non-Maxwellian Electron Populations in Non-LTE Simulations of Laser-Plasma Thermal and Implosion Experiments," to be published in the *Journal of Quantitative Spectroscopy and Radiative Transfer.*

A. Simon, W. Seka, L. M. Goldman, and R. W. Short, "Raman Scattering in Inhomogeneous Laser Produced Plasma," to be published in *Physics of Fluids.*

M. C. Richardson, R. Epstein, O. Barnouin, P. A. Jaanimagi, R. Keck, H. Kim, R. S. Marjoribanks, S. Noyes, J. M. Soures, and B. Yaakobi, "Multibeam, Laser-Imploded Cylindrical Plasmas," to be published in *Physical Review A.*

A. Hauer, R. D. Cowan, B. Yaakobi, O. Barnouin, and R. Epstein, "Absorption Spectroscopy Diagnosis of Pusher Conditions," to be published in *Physical Review.*

R. Epstein and R. S. Craxton, "Statistical Ray Tracing in Plasmas with Random Density Fluctuations," to be published in *Physical Review A.*

B. Yaakobi, "X-Ray Diagnostic Methods for Laser Imploded Targets" and "Thermal Transport, Mass-Ablation, and Preheat in Laser-Target Experiments," to be published in the *Proceedings of the Spring College on Radiation in Plasmas*, Trieste, Italy, June 1985 (World Scientific Publishing Co.).

Conference Presentations

The following presentations were made at the Boulder Damage Symposium, Boulder, CO, October 1985.

K. A. Cerqua, B. L. McIntyre, and W. Zhong, "Ion Exchange Strengthening of Nd-Doped Phosphate Laser Glass."

L. Bangjun, D. J. Smith, and B. L. McIntyre, "The Development of Nodular Defects in Optical Coatings."

D. J. Smith, B. Krakauer, C. J. Hayden, A. W. Schmid, and M. J. Guardalben, "Yttrium-Oxide-Based Anti-Reflection Coating for High Power Lasers at 351 nm."

G. A. Mourou, "Generation and Amplification of Femtosecond Pulses at kHz Repetition Rate," presented at the Topical Meeting on Optical Data Storage of the Optical Society of America, Washington, DC, October 1985 (invited talk).

G. A. Mourou, "The Frontier of Science: Femtosecond Pulses and Their Applications," presented at the 1985 Meeting of Corporate Associates of

the American Institute of Physics held at Eastman Kodak Research Laboratories, Rochester, NY, October 1985 (invited talk).

The following presentations were made at the Seventeenth International Workshop on Laser Interaction and Related Plasma Phenomena, Monterey, CA, October 1985:

M. C. Richardson, O. Barnouin, J. Delettrez, G. Gregory, L. Goldman, R. L. Hutchison, P. Jaanimagi, R. Keck, T. Kessler, H. Kim, S. Letzring, F. Marshall, R. L. McCrory, P. McKenty, D. Robacks, W. Seka, S. Skupsky, J. M. Soures, C. P. Verdon, B. Yaakobi, S. Lane, and S. Prussin, "Ablatively Driven Targets Imploded with the 24-UV-Beam OMEGA System."

M. C. Richardson, G. G. Gregory, R. L. Keck, S. A. Letzring, R. S. Marjoribanks, F. Marshall, G. Pien, J. Wark, B. Yaakobi, P. D. Goldstone, A. Hauer, G. S. Stradling, B. L. Henke, and P. A. Jaanimagi, "Time-Resolved X-Ray Diagnostics for High Density Plasma Physics."

B. Yaakobi, "X-Ray Diagnostics and X-Ray Laser Experiments at LLE."

The following presentations were made at the Twenty-Seventh Annual Meeting of the Division of Plasma Physics of the American Physical Society, San Diego, CA, November 1985:

O. Barnouin, J. Delettrez, R. Epstein, L. M. Goldman, S. Letzring, M. C. Richardson, J. M. Soures, B. Yaakobi, A. Hauer, and P. A. Jaanimagi, "Transport Experiments in 24-Beam UV Irradiation of Spherical Targets."

B. Boswell, J. Delettrez, and L. M Goldman, "Analytical Modeling of Spherical UV Laser-Driven Ablation with Arbitrary Flux Limiter."

R. S. Craxton, J. Delettrez, R. L. Keck, R. L. McCrory, M. C. Richardson, W. Seka, and J. M. Soures, "Simulations of Absorption at 351 nm on Spherical Targets."

J. Delettrez, O. Barnouin, R. Epstein, P. Holstein, P. Jaanimagi, S. Skupsky, and K. Swartz, "Interpretation of Spherical Thermal Electron Transport Experiments on the 24-Beam UV OMEGA Laser System."

R. Epstein, J. Delettrez, S. Skupsky, R. Marjoribanks, B. Yaakobi, and P. A. Jaanimagi, "Simulation of Time-Resolved Spectra from Spherical Thermal Transport Experiments on the 24-Beam UV OMEGA Laser System."

S. R. Goldman, W. C. Mead, J. A. Cobble, D. Delamater, P. D. Goldstone, R. S. Marjoribanks, F. J. Marshall, M. C. Richardson, and G. Stradling, "Physics of High-Z Laser Target Interactions at $\lambda = 0.35\ \mu$m."

G. Gregory, S. Letzring, and M. C. Richardson, "Time-Resolved Photography of Uniformly Irradiated Spherical Targets at 351 nm."

P. A. Jaanimagi, B. L. Henke, O. Barnouin, J. Delettrez, R. Epstein, M. C. Richardson, B. Yaakobi, and A. Hauer, "Thermal Transport: A Comparison between Solid and Shell Targets."

R. L. Keck, D. M. Roback, L. M. Goldman, R. L. McCrory, P. W. McKenty, M. C. Richardson, J. M. Soures, and C. P. Verdon, "Target ρR Measurements of Implosions Driven by UV OMEGA."

S. A. Letzring, G. Pien, L. M. Goldman, M. C. Richardson, and J. M. Soures, "A Neutron Time-of-Flight Diagnostic with High Time Resolution."

R. S. Marjoribanks and M. C. Richardson, "Development of a High Resolution Collecting-Crystal Streak Spectrograph for Laser-Plasma Studies."

R. S. Marjoribanks, M. C. Richardson, G. Pien, O. Barnouin, B. Yaakobi, G. Stradling, A. Hauer, J. Cobble, P. D. Goldstone, S. R. Goldman, W. C. Mead, P. A. Jaanimagi, and B. Henke, "Time-Resolved M-Line Studies of Uniformly Irradiated Au Laser Plasmas."

F. J. Marshall, J. Delettrez, R. Epstein, P. W. McKenty, M. C. Richardson, J. M. Soures, and C. P. Verdon, "The Spatial Distribution of X-Ray Emission from Laser Fusion Targets."

R. L. McCrory, "Progress in Laser Fusion with Submicron Lasers" (invited review).

P. W. McKenty, C. P. Verdon, M. C. Richardson, J. Delettrez, F. J. Marshall, R. L. McCrory, and J. M. Soures, "Numerical Simulation of Recent 24-Beam Blue (351-nm) OMEGA Implosions."

C. J. McKinstrie and A. Simon, "Nonlinear Saturation of the Absolute Raman Instability in a Finite Collisional Plasma."

G. Pien, M. C. Richardson, P. Goldstone, F. Ameduri, and G. Eden, "Computerized Multichannel GHz Soft X-Ray Spectrometry on OMEGA."

M. C. Richardson, R. L. Keck, S. Letzring, R. L. McCrory, P. W. McKenty, D. Roback, J. M. Soures, C. P. Verdon, and S. M. Lane, "High-Yield and High-Density Target Implosions Driven by UV OMEGA."

W. Seka, S. Batha, L. M. Goldman, A. Simon, and R. Bahr, "Raman Up-Scattering and Down-Scattering in Laser Produced Plasmas Using 527-nm Radiation."

R. W. Short, "Self-Focusing and Uniformity in Laser-Fusion Target Illumination."

A. Simon, R. W. Short, L. M. Goldman, and W. Seka, "Further Applications of the Enhanced Plasma Noise Model of Raman Scattering."

S. Skupsky, J. Delettrez, and M. Sapir, "Non-Local, Non-Maxwellian Effects in Laser-Produced Plasmas."

J. M. Soures, R. Hutchison, S. Jacobs, R. Keck, T. Kessler, S. Letzring, R. L. McCrory, M. C. Richardson, and W. Seka, "The OMEGA, 24-Beam, 2.4-kJ, Ultraviolet Laser System: Initial Operation and Performance Characterization."

K. Swartz, R. W. Short, and A. Simon, "The Effect of Multiple Beams on Parametric Instabilities."

C. P. Verdon, R. L. McCrory, P. W. McKenty, and S. Skupsky, "Effects of Long-Wavelength Nonuniformities on High-Gain ICF Pellet Implosions."

J. S. Wark, M. C. Richardson, B. Yaakobi, and A. Hauer, "Spatially Resolved X-Ray Absorption Spectroscopy."

B. Yaakobi, A. Hauer, O. Barnouin, P. A. Jaanimagi, R. Epstein, R. L. McCrory, M. C. Richardson, and J. M. Soures, "X-Ray Absorption-Lines Measurement of the Tamper ρR and Temperature."

The following presentations were made at the First International Laser Science Conference, Dallas, TX, November 1985:

M. C. Richardson, "X-Ray Laser Studies with Line-Focused Laser Plasmas" (invited paper).

B. Yaakobi, S. Letzring, J. M. Soures, F. J. Marshall, M. C. Richardson, C. B. Collins, and S. S. Wagel, "Laser-Generated X-Ray Source for Pumping Nuclear Transitions."

The following presentations were made at the American Vacuum Society Conference, Houston, TX, November 1985:

R. Q. Gram, H. Kim, J. F. Mason, and M. Wittman, "Ablation-Layer Coating of Mechanically Nonsupported Inertial Fusion Targets."

H. Kim, S. Noyes, M. C. Richardson, and B. Yaakobi, "Fabrication of Thin Cylindrical Targets for X-Ray Laser Fusion."

R. L. McCrory, "Progress and Promise for Direct-Drive Short-Wavelength Laser Fusion, presented at the 17th European Conference on Laser Interaction with Matter, Rome, November 1985 (invited talk).

G. A. Mourou, "Applications of Picosecond Electron Diffraction to the Study of Structural Phase Transititon," and "Ultra-High-Speed Opto-electronics," presented at Lasers '85, Society for Optical and Quantum Electronics, Las Vegas, NV, December 1985 (invited talks).

G. A. Mourou, "Femtosecond Optical Techniques for the Characterization of Present and Future Ultrafast Electronic Devices," presented at the Workshop on Ultrasmall and Quantum-Structured Devices, Tempe, AZ, December 1985 (invited talk).

ACKNOWLEDGMENT

The work described in this volume includes current research at the Laboratory for Laser Energetics, which is supported by Empire State Electric Energy Research Corporation, General Electric Company, New York State Energy Research and Development Authority, Ontario Hydro, Southern California Edison Company, the University of Rochester, and the U.S. Department of Energy Office of Inertial Fusion under agreement No. DE-FC08-85DP40200.